LBL-13659

Lawrence Berkeley Laboratory
UNIVERSITY OF CALIFORNIA

Materials & Molecular
Research Division

THE EFFECTS OF OXYGEN ON THE MICROSTRUCTURE OF $Cu_{2-x}S$ THIN FILMS

Timothy David Sands
(M.S. thesis)

November 1981

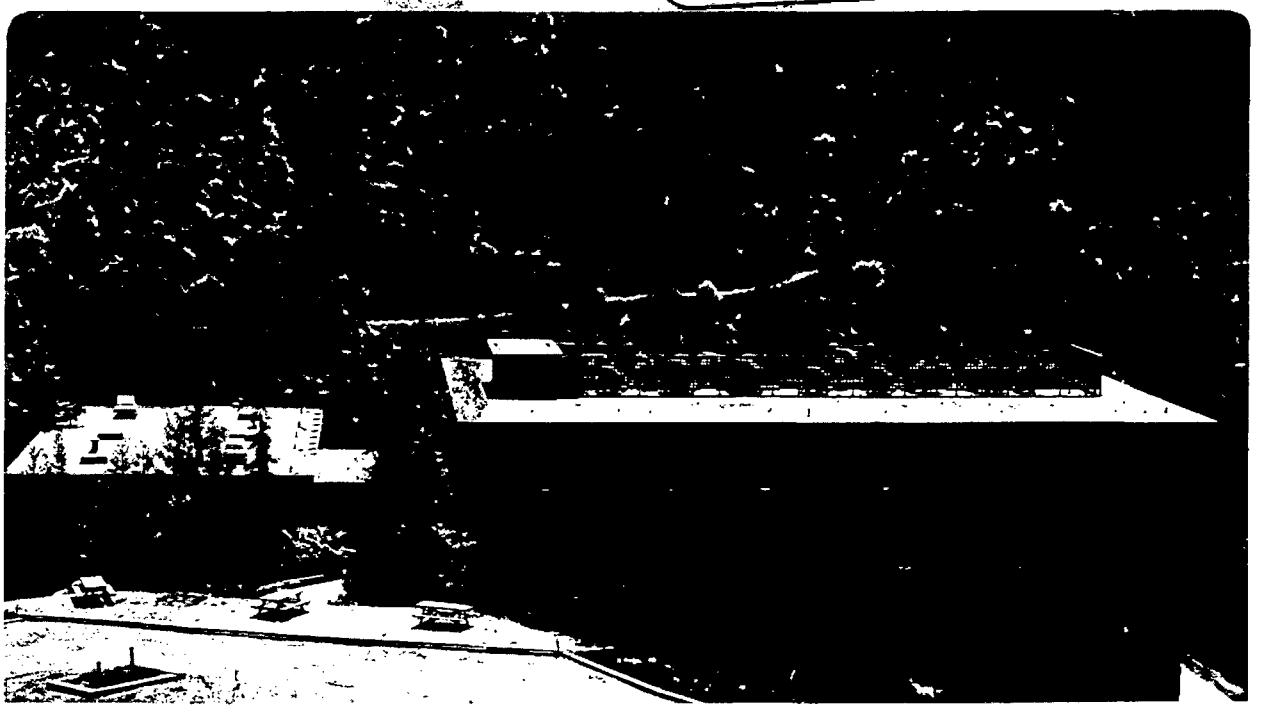

Prepared for the U.S. Department of Energy under Contract W-7405-ENG-48

DISCLAIMER

THE EFFECTS OF OXYGEN ON THE MICROSTRUCTURE OF $Cu_{2-x}S$ THIN FILMS

Timothy David Sands

Materials and Molecular Research Division

Lawrence Berkeley Laboratory

and

Department of Materials Science and Mineral Engineering

University of California

Berkeley, California 94720

This work was supported by the Director, Office of Energy Research, Office of Basic Energy Sciences, Division of Materials Sciences of the U. S. Department of Energy under Contract No. W-7405-ENG-48.

THE EFFECTS OF OXYGEN ON THE MICROSTRUCTURE OF $Cu_{2-x}S$ THIN FILMS

Table of Contents

THE EFFECTS OF OXYGEN ON THE MICROSTRUCTURE OF $Cu_{2-x}S$ THIN FILMS

Timothy David Sands

Materials and Molecular Research Division

Lawrence Berkeley Laboratory

and

Department of Materials Science and Mineral Engineering

University of California

Berkeley, California 94720

ABSTRACT

Changes in the microstructure of $Cu_{2-x}S$ thin films after heat treatments in air at 180°C were monitored by high resolution transmission electron microscopy (TEM). Specimens were prepared by the aqueous exchange of copper and cadmium in the surface layers of pre-thinned CdS single crystals, simulating the copper sulfide layer in $Cu_{2-x}S$/CdS solar cells without the complicating influence of CdS grain boundaries.

Results indicate that the oxidation of copper and the oxidation of sulfur are competing processes which depend on the temperature range of the heat treatment. A kinetic model explaining this behavior is proposed, wherein the effects of the activation barrier opposing the hexagonal chalcocite to cubic digenite transformation are recognized. A sequence of "superstructure images" indicating a net sulfur loss in $Cu_{2-x}S$ during heat treatment is presented in support of this model.

Furthermore, observations of the $Cu_{2-x}S$ microstructure reveal that

chalcocite/djurleite interfaces are abrupt to within 20Å. The structural relationships between these two phases are examined in detail and a possible transformation mechanism involving the clustering of copper vacancies is presented. In addition, the chalcocite in the vicinity of chalcocite/djurleite interfaces was found to contain a high density of 1/4 [010] faults. Structural considerations show that these faults are likely sites for copper vacancies.

Finally, the consequences of these results for solar cells based upon $Cu_{2-x}S$ layers produced by the aqueous exchange method are discussed with emphasis on long-term degradation and processing heat treatments conducted in air.

I. INTRODUCTION

A. Objective

The decreasing availability and increasing cost of non-renewable energy sources make the search for new energy forms an urgent and essential activity. Of increasing importance is the need to establish a diverse profile of renewable resources, including various forms of solar power. A promising candidate in this category is the photovoltaic cell, a device which effectively converts the power in incident solar photons to usable electric power.

This direct conversion of light to electricity has proven useful for space applications in recent decades but its adaptation to terrestrial environments is not yet complete. The terrestrial adaptation of one particularly promising device, the $Cu_{2-x}S$/CdS thin-film solar cell, is hampered by a lack of understanding of the effects of air on the complicated phase relationships of copper sulfide.[1] Thus, before a copper sulfide layer with optimum stoichiometry and improved stability can be logically developed, the reactions between $Cu_{2-x}S$ and air must be clearly understood.

This study encompasses the structural aspect of the copper sulfide-air interaction by using phase contrast transmission electron microscopy to directly observe

the microstructural changes in $Cu_{2-x}S$ which occur during exposure to air under conditions similar to those encountered during processing and operation of a solar cell.

B. The Photovoltaic Effect in p-n Junction Solar Cells.

1. The Mechanism.

A basic understanding of the photovoltaic effect is necessary for both the design of new solar cell materials and the improvement of materials already employed in photovoltaic devices. The mechanism of the photovoltaic effect described briefly in this section is discussed in depth by K. W. Boer[2], R. H. Bube[3], and H. J. Hovel[4].

The photovoltaic effect is a consequence of the separation of charge by the diffusion potential created by the joining and equilibration of two semiconductors of opposite electronic conductivity type. When n and p semiconductors make contact, small fractions of majority carriers from each side diffuse through the junction to the opposite side where they become minority carriers, thereby increasing the entropy of the semiconductor system. As each electron flows from n to p, it leaves behind a fixed positive charge on the n side of the junction with the analogous result for holes flowing from p to n. This double layer of charge produces a "built-in" electric field which opposes further diffusion.*

An impinging photon with energy greater than the semiconductor's bandgap can transfer its energy to an electron and a hole by exciting a valence electron into the conduction band, thus creating an electron-hole pair. Electrons in the p-type region and holes in the n-type region mobilized by this photoabsorption process can then

*An equivalent description in terms of the electrochemical potential shows that the height of the diffusion barrier at zero bias is slightly less than the magnitude of the semiconductor's bandgap (Eg) for a typical homojunction at room temperature.

lower their energies by crossing the p-n junction under the influence of the diffusion potential. The additional electric field created by these excess carriers opposes the built-in field. Therefore, the junction is forward-biased by a voltage no greater in magnitude than the diffusion potential. External loading and internal (including contact) resistances reduce the net forward voltage across the device.

Recombination processes dictate that only those minority carriers generated within a diffusion length of the junction have a high probability of crossing the p-n interface to be collected by an external circuit (note that this photogenerated current is opposite in direction to the current from an unilluminated forward-biased diode). The product of this current with the voltage across the device is the usable power successfully converted from the incident power of the solar photons.

2. Materials Considerations

The suitability of a semiconducting material for photovoltaic energy conversion depends upon the many interrelated parameters described in this section (see references 2, 3, and 4).

As incident photons begin to interact with one of the semiconducting layers, the optical reflectivity, absorption spectrum, and bandgap of the material become important. A bandgap of approximately 1.4 eV is optimum for an incident solar spectrum on earth. Such a bandgap minimizes the sum of the losses from incomplete absorption and excess carrier energy. The details of the absorption spectrum depend on the individual spectra of the semiconducting layers and the junction region. Steep absorption edges normally indicate a direct bandgap material while sloping edges are characteristic of indirect bandgaps. Peaks in the absorption spectrum may also be due to effects such as photoconductivity of the junction region.

The overall absorption of photons incident on the solar cell can usually be enhanced by minimizing the optical reflectivity of the semiconductor with suitable coatings or by increasing the effective surface or junction area with chemical treatments.

Electrons and holes mobilized by the absorbed photons and moving toward the junction are influenced by the surface recombination velocity, the minority carrier diffusion length, the type of conductivity, the carrier mobilities and several other interrelated parameters. All of these properties depend greatly on impurities, defects, grain boundaries and nonstoichiometry in the case of compound semiconductors. Since electrons generally have longer minority carrier diffusion lengths than holes, solar cells are often designed so that most of the photon absorption takes place in the p-type material where electrons are the minority carriers.

As the mobile carriers approach the junction region of a heterojunction structure (in which the p and n semiconductor materials are different), they may encounter defects or lattice strain due to the lattice mismatch between the different semiconductors. The detrimental effects of these potential recombination sites can be minimized in some cases by alloying to alter one or both lattice parameters. The heterojunction band structure may also include a band spike at the interface due to the mismatch in properties such as electron affinities and bandgaps. This band spike prevents transport across the junction for those carriers which are not able to quantum mechanically tunnel through it.

Once past the junction region the carriers must move through the bulk of the remaining semiconductor and overcome the contact resistance to be collected by the external circuit. In theory, low resistance contacts to n-type semiconductors are possible if the work function of the semiconductor is greater than the work function of the contact metal (p-type semiconductors require $\phi_s < \phi_m$). However, real metal-semiconductor interfaces contain impurities and surface states which may prohibit the formation of a low resistance contact unless additional treatments are applied. In practice, many contacts are made by alloying or by heavily doping the semiconductor before metallization to produce a sufficiently narrow Schottky barrier depletion region so that it may be easily crossed by tunneling.

A semiconducting material in p-n homojunction configuration (p and n regions of the same material) or a pair of materials in heterojunction configuration must also meet the thermal and chemical stability requirements of terrestrial use. The semiconductor materials and contact metals should have similar coefficients of thermal expansion to minimize thermal cycling effects. Certainly, photochemical stability is important, especially for materials used in concentrator systems. In addition, chemical stability in air is necessary since all inexpensive encapsulants are slightly permeable to oxygen and water vapor and are subject to delamination. With the estimated necessary lifetime of approximately twenty years for ten percent efficient terrestrial solar cells, these stability requirements are perhaps the most difficult to satisfy.

On a broader scale, one must also include availability, low cost, and low toxicity as necessary or desirable qualities of solar cell semiconducting materials.

3. Specific Photovoltaic Systems

In recent years dozens of semiconducting materials in homojunction or heterojunction configuration have been found to exhibit the photovoltaic effect. However, no photovoltaic materials system is without serious economic or physical problems nor has any single material or system emerged as a clear leader.

The first solar cell to be extensively developed was the single crystal silicon homojunction used for power generation on satellites. Although expensive, this is the only commercially established system. The financial and energy costs involved in making silicon cells from single crystal ingots has limited this device to remote applications. However, dendritic, polycrystalline, and hydrogenated amorphous silicon devices show promise for larger scale development.

Gallium arsenide homojunctions and some related III-V heterojunction and homojunction systems (e.g. InP and GaAs/$Ga_xAl_{1-x}As$) have high efficiencies but they are also expensive and are most economically employed in concentrator systems.

$Cu_{2-x}S$/CdS solar cells represent a third class of photovoltaic material systems. In these devices nearly all of the photoabsorption and minority carrier production occurs in a thin p-type copper sulfide layer. $Cu_{2-x}S$/CdS thin-film polycrystalline heterojunctions can be manufactured by mass production techniques, making them particularly attractive. Cells of this type have recently surpassed ten percent efficiency in the lab,[1] however their poor long term stability in air prevents the use of inexpensive plastics as encapsulants. Instead, $Cu_{2-x}S$/CdS cells must be encapsulated in non-air-and-moisture-permeable glass, thus increasing the cost and weight of these devices. Further development of these cells is impeded by a lack of understanding of the $Cu_{2-x}S$ oxidation mechanisms during both long term use and processing heat treatments.

C. <u>The $Cu_{2-x}S$/CdS Solar Cell</u>.

1. Heterojunction Fabrication and Morphology.

The many methods for producing the n-type CdS layer, including thermal evaporation, spraying, screen-printing, and sputtering, are discussed in a review article by R. Hill.[5] A typical CdS layer fabricated by these methods is 5 to 30μm thick and consists of columnar grains of wurtzite structure with the c-axis nearly normal to the substrate. By doping techniques, film resistivities can be reduced to approximately 10 ohm-cm with electron mobilities up to 100 cm^2/volt-sec. and hole mobilities a factor of ten lower.

Before copper sulfide formation, the CdS layer is etched to yield a clean surface with pyramidal grain tops and slightly exposed grain boundary regions. The simplest and most developed method of $Cu_{2-x}S$ layer formation is the aqueous exchange of Cd^{++} and Cu^{+} ions in an agitated Cu_2Cl_2 solution at 90 to 98°C. High pH solutions yield a diffusion-limited $\sqrt{t}$ growth rate of topotaxial $Cu_{2-x}S$ in the surface layer of polycrystalline CdS. Solution etching of the CdS grain boundaries leads to a linear overall growth rate for low pH solutions.[6]

Typical copper sulfide layers produced by a 5 to 10 second dip are 0.1μm thick on the exposed surface with penetrations of 1 to 2μm down CdS grain boundaries (see Fig. 1). Although the vertical component of the copper sulfide layer substantially increases the effective junction area, grain boundary penetrations deeper than 1 or 2μm increase the chance of shorting to the substrate during cell operation. Consequently, plating baths with high pH values are generally preferred.

The composition of the resulting layer is critically dependent on the plating bath temperature and oxygen content. Oxidation of Cu^{+} to Cu^{++} in the plating solution is the major contributing factor to the formation of the undesirable copper sulfide, djurleite ($\sim Cu_{1.96}S$). This phase has a larger bandgap (1.8eV), a greater lattice mismatch with CdS[7], and a shorter minority carrier diffusion length[8] than chalcocite (Cu_2S, $E_{g,indirect}$ = 1.2 eV). Djurleite/CdS solar cells do not show an appreciable photovoltaic response so elimination of dissolved oxygen in the plating bath is essential to insure formation of efficient heterojunctions (i.e. chalcocite/CdS).

Although bath temperatures less than approximately 95°C also result in films containing djurleite, the temperature parameter is more easily controlled and does not present a serious problem. Heating the CdS substrate to ~100°C before dipping may improve control of the growth temperature and stoichiometry. However, this technique is as yet untested.

2. Processing Heat Treatments

Following the addition of the copper sulfide layer, the heterojunction is subjected to a poorly understood but effective heat treatment in air at 150 to 250°C for several minutes. Before this heat treatment, the heterojunction shows little, if any, photovoltaic response. During the first minutes of the air bake, the response increases rapidly and then peaks. Further heating results in a gradual decay of the photovoltaic efficiency.

The observed improvement in solar cell response has been explained by several mechanisms. Using spectral response measurements, Caswell, Russell and Woods[9] have shown that a short heat treatment at 200°C in air results in the formation of a copper-diffused photoconductive region in the CdS near the junction. The contribution of this region to the spectral response of the cell may be a partial explanation for the observed improvement in cell characteristics after heat treatment. The need for an air environment during treatment is generally attributed to the oxidation of a small amount of copper to form a layer of copper oxide, thereby creating a minority carrier rejection potential at the surface and reducing surface recombination losses.[10,11]

Both of these theories have a weakness in that they require the removal of copper from Cu_2S. As mentioned earlier, the presence of phases with reduced copper content such as djurleite ($\sim Cu_{1.96}S$) is detrimental to the solar cell characteristics. More reasonable explanations may involve the additional loss of sulfur reported by Arjona et al.[12] Two related hypotheses are the possible formation of cupric sulfate (Czanderna, Prince, and Hebig[13]) and the production of a $Cu_xS_yO_{1-y}$ semiconductor which acts as a window and reduced recombination losses at the surface (Loferski et al.[14]).

Further reasons for the enhanced photovoltaic characteristics after heat treatment may be the homogenization of the Cu_2S layer during annealing and the compensation of $Cu_{2-x}S$ by diffused cadmium.[15]

The mechanism of degradation during prolonged heating in air is more uniformly agreed upon; as more copper is removed from the copper sulfide by oxidation (or by reaction with CO_2 and H_2O), the amount of djurleite increases until the photovoltaic response of the heterojunction is severely reduced. Subsequent exposure to a reducing atmosphere is well known to at least partially restore the Cu_2S stoichiometry.[11,16].

Bogus and Mattes have developed a method to curtail the copper loss from Cu_2S during heat treatment by the pre-treatment evaporation of a thin layer of copper.[17] This procedure insures the Cu_2S stoichiometry; however, for optimum results the amount of copper evaporated and the duration of the following heat treatment must be individually tailored to each specimen.

3. Long-Term Degradation

The instability of the $Cu_{2-x}S$/CdS solar cell during terrestrial operation is due predominantly to degradation processes in the copper sulfide. Investigators have proposed three mechanisms as major contributing factors.

First, the oxidation of chalcocite to djurleite by air and moisture which penetrates the encapsulation is frequently cited as a major mode of degradation[18,19,20,21].

A second possible mechanism is the transformation of chalcocite to djurleite driven by the copper depletion resulting from Cu diffusion into bulk CdS[21].

The third prominent degradation mechanism involves the eventual production of Cu filaments by field-assisted-diffusion down CdS grain boundaries while the cell is subjected to moderate electrical loading.[20,21,22] These filaments cause shorting between $Cu_{2-x}S$ and the substrate, thereby reducing the open circuit voltage and fill factor (F.F. = max. power/Voc.Isc) of the cell.

All three mechanisms result in the conversion of chalcocite to djurleite and the corresponding reduction in short circuit current generated by the cell.

D. Copper Sulfide Phase Relationships.

1. Chalcocite, Djurleite, and the Tetragonal Phase.

Both chalcocite and djurleite are composed of an ordered superlattice of copper within a distorted hexagonal-close-packed sulfur sublattice. Above 104°C the copper atoms in Cu_2S become disordered. However, below 435°C the hexagonal-close-packed sulfur sublattice is retained.[23,24,25] This disordered phase is hexa-

gonal (space group $P6_3/mmc$) with $a_{hex} = 3.95$ Å and $c_{hex} = 6.75$ Å.[26]

Equilibrium phase diagram determination has been hampered by the appearance of several metastable phases and the kinetic effects associated with them[23,24,25]. The most accurate results to date have come from electrochemical measurements by Potter.[23] His version of the Cu-S phase diagram (Fig. 2) illustrates the extreme structural sensitivity of $Cu_{2-x}S$ to small deviations in stoichiometry from $Cu_{2.000}S$, especially near the order-disorder transition temperatures (90-104°C). In particular one can delineate at least five different compositional regimes at 25°C in the range $1.942 < 2-x < 2.000$, each with a different predicted bulk behavior upon slow heating and cooling (see Fig. 2).

Rapid temperature variation, impurities, and mechanical specimen preparation methods can all result in the formation of metastable phases of which tetragonal $Cu_{2-x}S$ is the most common.[23] The composition of this phase is approximately $Cu_{1.96}S$, however the structure is not known. Lattice parameters measured by Djurle are $a = 4.008$ Å and $c = 11.268$ Å.[27] This metastable phase probably has an effect on the outcome of heat treatments at 150 to 250°C given to $Cu_{2-x}S$/CdS solar cells since the tetragonal phase is generally formed in the temperature range of 100 to 150°C. As suggested by Potter,[25] in this temperature range the formation of the metastable tetragonal phase may be preferred to the formation of a stable digenite-hexagonal chalcocite mixture due to the large activation barrier encountered in the conversion of chalcocite (with a roughly h.c.p. sulfur sublattice) to digenite (with a roughly c.c.p. sulfur sublattice). This activation barrier may also be responsible for a substantial fraction of the observed improvement in the $Cu_{2-x}S$/CdS solar cell characteristics after heating in air above 150°C. This point will be examined in the discussion of the results presented in this paper.

The structure of the stable low temperature phases, djurleite and low chalcocite, are still in question. However, x-ray work by Evans[28,29] has yielded results

which are reasonable but complicated. Evans found that low chalcocite is monoclinic with a space group of either $P2_1/c$ or Pc and the following unit cell parameters:

$a = 15.25\ \text{Å}$

$b = 11.88\ \text{Å}$

$c = 13.49\ \text{Å}$

$\beta = 116.35°$

cell content: 48 Cu_2S.

The c-axis coincides with the c-axis of the sulfur sublattice while b is approximately three times the hexagonal sublattice parameter "a_{hex}". Djurleite ($Cu_{1.938}S$) was also found to be monoclinic with space group $P2_1/n$ and the following unit cell parameters:

$a = 26.90\ \text{Å}$

$b = 15.75\ \text{Å}$

$c = 13.57\ \text{Å}$

$\beta = 90.13°$

cell content: 248 Cu, 128 S.

The a-axis coincides with the c-axis of the sulfur sublattice while b is approximately four times the hexagonal sublattice parameter "a_{hex}".

Electrochemical measurements by Potter[23] indicate that djurleite is a solid solution with (2-x) varying from 1.965 to 1.934. Since one copper vacancy in the asymmetric unit of djurleite yields a composition of $Cu_{1.969}S$ while two vacancies yield a composition of $Cu_{1.938}S$, it is reasonable to consider djurleite to be a superstructure resulting from the ordering of copper vacancies in low chalcocite. The structure of $Cu_{1.969}S$ has not been reported, presumably because it is very difficult to isolate this phase from chalcocite and $Cu_{1.938}S$[28] (as would be required for conclusive x-ray diffraction measurements). However, lattice parameter

measurements by electron diffraction of Cu-rich djurleite coherently intergrown with chalcocite yield values similar to those reported by Evans for $Cu_{1.938}S$ (see Results). The details of the chalcocite and djurleite structures will be examined further in the discussion.

The structural relationships between chalcocite and djurleite are difficult to visualize with the unit cells described above. Fortunately, both phases can be adequately described with simple pseudo-orthorhombic unit cells which clearly reveal geometrical relationships. Thus, the following approximate unit cell conventions will be used for the remainder of the paper:

chalcocite	a'	= 11.9Å
	b'	= 27.3Å
	c'	= 13.5Å
djurleite	a'	= 15.7Å
	b'	= 13.6Å
	c'	= 26.9Å .

With these conventions the following relationships hold with respect to the lattice parameters of high-temperature hexagonal chalcocite:

chalcocite	a'	$\tilde{=} 3 \cdot a_{hex}$
	b'	$\tilde{=} 4\sqrt{3} \cdot a_{hex}$
	c'	$\tilde{=} 2 \cdot c_{hex}$
djurleite	a'	$\tilde{=} 4 \cdot a_{hex}$
	b'	$\tilde{=} 2\sqrt{3} \cdot a_{hex}$
	c'	$\tilde{=} 4 \cdot c_{hex}$.

From the above relationships, it is evident that the pseudo-orthorhombic unit cells of both chalcocite and djurleite can have any of three orientations at ~ 120° intervals about the c-axis in a fixed h.c.p. sulfur sublattice (see Fig. 3). However, the distortion of the actual sulfur sublattice makes certain orientational combinations of the two phases more compatible than others (see Discussion).

2. Electron Microscopy of the Chalcocite-Djurleite Transformation

The structural compatibility of low chalcocite and djurleite, and the small difference in composition between these two phases makes macroscopic studies of their structure and transformations ambiguous. The chalcocite-djurleite transformation has not, to the author's knowledge, been studied previously in real space at a microscopic level. However, an electron diffraction experiment involving this transformation has been reported by A. Putnis[26]. He observed the behavior of copper sulfide specimens of unknown composition when heated by the electron beam. As he monitored electron diffraction patterns of the same areas through heating and cooling cycles, Putnis noted that the two phases, chalcocite and djurleite, seemed to form with nearly equal likelihood upon cooling, regardless of the initial phase. Putnis concludes: "The transformation sequence clearly implies that the chalcocite and djurleite superstructures can exist at the same chemical composition."

Although his results may be important, there is some question about the validity of his interpretation. First, as the results presented in this paper show, chalcocite and djurleite can be coherently intergrown with superlattice grain dimensions varying from a few hundred angstroms to several thousand angstroms. Therefore, a two phase mixture, when heated above the order-disorder transformation temperature and then cooled, can have a resulting microstructure with an entirely different spatial arrangement of the two phases (requiring only a small amount of Cu ion movement), while preserving the same <u>average</u> composition.

Second, Putnis reports that he was able to monitor the diffraction pattern from the same 1000Å diameter area through the thermal cycles using a selected area aperture. However, the uncertainty in locating a selected area aperture is typically 350Å (on the specimen plane) due to spherical aberration of the objective lens[30]. In addition, the necessary adjustment of the specimen position after beam heating introduces further uncertainties.

To avoid these difficulties and their associated ambiguities, the technique of phase contrast transmission electron microscopy was chosen to monitor the microstructure of $Cu_{2-x}S$ in both real space and reciprocal space. An added benefit of this method is that TEM specimens are generally several hundred to several thousand angstoms thick, the same thickness range as that of typical $Cu_{2-x}S$ layers in $Cu_{2-x}S$/CdS solar cells. Results should therefore be representative of actual changes in the copper sulfide layer of the solar cell, although the kinetics will be enhanced by the additional free surface.

II. EXPERIMENTAL METHOD

In order to avoid the complications of CdS grain boundaries in this initial study, bulk single crystals of undoped CdS (Eagle-Picher) were used as the starting material. Transmission electron microscope specimens of CdS were fabricated by orienting the crystal with the Laue x-ray technique ((0001) orientation), sectioning the CdS with a diamond saw, and then mechanically and chemically polishing the specimen to a thickness of approximately 50μm[31]. The final thinning was accomplished by argon ion milling to electron transparency.

Immediately prior to electron microscope examination, a freshly ion milled CdS specimen was etched for 5-10 seconds in 37% HCl and then dipped in the ion exchange bath for 30 seconds. The resulting topotaxial reaction usually converted the entire thin area (transparent to 100keV electrons) to $Cu_{2-x}S$.

The ion exchange bath was prepared by first boiling 250ml of de-ionized H_2O for approximately 15 minutes in a covered and vented pyrex flask. A thermometer and an argon bubbler were then inserted through air-tight stoppers in two necks of the flask. The argon gas served to help purge the bath of dissolved oxygen and to agitate the solution during the conversion process. Following the purification step, 1.5 grams of 99.999% Cu_2Cl_2 and 0.5 grams of NaCl reagent were added to the

bath[32]. The solution temperature was then stabilized at a previously chosen temperature between 90 and 99°C. As in the actual photovoltaic devices, the $Cu_{2-x}S$ layers produced by this method probably contained a small concentration of cadmium interstitials near the $Cu_{2-x}S$/CdS interface which were left behind at the end of the exchange process[33]. However, only regions entirely converted to $Cu_{2-x}S$ were examined in this study. Consequently, the concentration of cadmium was probably negligible (from a structural standpoint).

Immediately after conversion to $Cu_{2-x}S$, the specimen was rinsed in de-ionized water and allowed to dry in air. Once dry, the $Cu_{2-x}S$/CdS specimen was inserted into a Siemens 102 transmission electron microscope operated at 100kV. Phase contrast electron microscopy (described in the appendix) was used to obtain a "superstructure image" of a desired area in (001) orientation. The specimen was then removed from the microscope, given a heat treatment in air, and reinserted into the microscope column. After relocating the same area of the specimen, another superstructure image was recorded in the same orientation. This procedure could be repeated several times. However, specimen-borne contamination severely limited the visibility of the high resolution image after the third insertion into the microscope. Methods of removing the contamination layer (such as ion milling) were avoided since these procedures would have altered the area to be examined.

III. RESULTS

All microscopy in this study was done in [001] zone axis orientation. The (100) plane spacings of chalcocite (~12Å) and djurleite (~16Å) are indicated on the micrographs described below.

A. Diffraction Patterns

A typical diffraction pattern obtained from a sample containing both chalcocite and djurleite is indexed in Fig. 4. The spot directly left of the central beam in Fig. 4b is the 040 spot of chalcocite (referenced to the pseudo-orthorhombic

unit cell outlined in Fig. 3). In a c'-axis projection the chalcocite structure appears to have a repeat distance of approximation 13.6Å along [010], consequently one would expect to observe an 020 spot also (provided the structure factor and dynamical diffraction requirements were satisfied). However, the 020 spot was found to be replaced by a streak in Fig. 4a, indicating a variation in the repeat distance along the [010] axis.

Also shown in Fig. 4a is the shadow of the objective aperture used throughout this study. Note that the aperture does not include the sulfur sublattice spots. All high resolution images presented are therefore superstructure images which contain no direct information from the sulfur sublattice.

B. Changes in the Microstructure During Exposure to Air.

A copper sulfide film was formed on a pre-thinned CdS TEM specimen by dipping the CdS into an ion exchange bath (described in the Experimental Method section) for 30 seconds at 95 ± 1°C. Fig. 5a is a "superlattice image" of a portion of the film near the edge of the foil. Careful examination of this image and the corresponding diffraction pattern revealed a microstructure consisting of similar amounts of chalcocite and djurleite (diffraction information was gathered from an area of approximately 5000Å diameter centered on the region imaged in Fig. 5a).

After a 15 minute heat treatment in air at 180 ± 5°C, the specimen was re-examined. A "superlattice image" and a diffraction pattern from the same area are shown in Fig. 5b. Note the formation of voids and the increased fraction of chalcocite.

Fig. 5c shows the microstructure after four days in air (shielded from light) at approximately 20°C. All of the chalcocite and one orientational variant of djurleite have reordered into a fairly uniform region of djurleite. At this point no further experimentation with this sample was possible due to a thickening contamination layer.

The sequence of microstructural changes described above is mapped out in Fig. 6.

Fig. 7 illustrates the effect of air on a second copper sulfide film prepared by the same method (bath temperature = 98°C). Immediately following the $Cu_{2-x}S$ layer formation, the thin area of the specimen was examined in diffraction and found to be entirely chalcocite. After a 20 minute bake in air at 80 $\pm$ 5°C, the specimen was reinserted into the microscope for superstructure imaging. Fig. 7a shows the chalcocite superstructure with no evidence of djurleite. However, heating to 180°C in air for 5 minutes resulted in a $Cu_{2-x}S$ microstructure composed exclusively of djurleite (Fig. 7b).

C. Chalcocite/Djurleite Interfaces

Several images of interfaces between chalcocite and djurleite were recorded during the above experiments. Fig. 8 is a high magnification image of the upper right region of Fig. 5a. Also, the diffraction pattern corresponding to Figs. 8 and 5a is the indexed pattern of Fig. 4b.

Various other interface orientations are illustrated in Figs. 9, 10, and 11. Fig. 10 is an enlargement of the upper left corner of Fig. 5b. Note that this is the only image of an interface with $[100]_{chalcocite}$ parallel to $[100]_{djurleite}$ (along with Fig. 12 which is from an adjacent area). Of interest in Fig. 11 is the variation in periodicity along the [010] direction of chalcocite. It appears that the regular periodicity of 13.6Å is occasionally interrupted by one or more 6.8Å spacings. Both Figs. 11 and 12 are from the same through-focal-series as Fig. 5b. Variations in [010] spacings are also evident in Fig. 12. The possible relationship between these variations and the chalcocite-djurleite transformation will be examined in the discussion.

IV. DISCUSSION

A. The Effects of Oxygen: Consequences for Solar Cells

The results displayed in Figs. 5 and 6 suggest that the improvement of $Cu_{2-x}S$/CdS solar cell characteristics after heat treatment may be partly due to sulfur loss with the promotion of djurleite to chalcocite upon cooling. As mentioned in the Introduction, the prevailing opinion among investigators of $Cu_{2-x}S$-air interactions is that copper is oxidized during heat treatment to form Cu_yO, thereby creating a minority carrier rejection potential at the surface. Certainly, at temperatures less than 100°C, the removal of copper from the sulfur sublattice is the predominant effect of air on $Cu_{2-x}S$. However, examination of the Cu-S phase diagram indicates that at temperatures above 100°C, oxidation effects may be influenced by the activation barrier of the hexagonal chalcocite to cubic digenite transformation (see Fig. 2).

Note that the situation is by no means a simple bulk equilibrium between copper and sulfur; thin film surface effects and the presence of oxygen, water vapor, and CO_2 must also be recognized. Therefore, a Cu-S equilibrium phase diagram is only useful qualitatively and with reservations. However, the following qualitative points are probably applicable to the copper sulfide films (excluding the exposed surfaces) produced for this study:

i. Above 100°C, copper sulfide ($2-x < 2$) would prefer to exist as a mixture of hexagonal chalcocite and cubic digenite

and,

ii. As $x \longrightarrow 0$, ($T > 100$°C), copper sulfide has less tendency to assume the cubic digenite structure.

If these two general statements apply to the thin film Cu-S case (excluding the exposed surface), then it is likely that the large activation barrier expected for the h.c.p. to c.c.p. sulfur sublattice transformation will have significant effects on the

results of heat treatments in air. These effects are described below as a function of temperature.

A chalcocite-djurleite mixture heated above 150°C may lower its free energy by converting to a mixture of hexagonal chalcocite and cubic digenite. However, the large activation barrier generally encountered as an h.c.p. structure converts to c.c.p., impedes this transformation. Above 150°C a lower energy pathway to a more stable state may involve the release of sulfur so that the composition of $Cu_{2-x}S$ approaches Cu_2S where the drive to form digenite is much weaker.

In the range of approximately 100°C to 150°C, the tetragonal phase is believed to be a metastable state preferred by copper sulfides which are not supplied enough thermal energy to overcome the activation barrier in a reasonable amount of time.[25] For temperatures considerably above 150°C, the activation barrier is easily surmounted and compositions with $(2-x) < 2$ can be accommodated by a hexagonal chalcocite-cubic digenite mixture.

Therefore, a net sulfur loss can probably be achieved only if the temperature is between approximately 150°C and some limiting temperature, above which the h.c.p.-c.c.p. transformation proceeds with ease. The window region between these two temperatures would thus represent the desirable temperature range for heat treatments in air to improve stoichiometry.

The presence of oxygen probably acts to encourage sulfur loss by the formation of a compound such as $CuSO_4$, the production of which has been suggested by D. T. Rickard[34], and Czanderna, Prince, and Hebig.[13] In fact, D. T. Rickard reported that chalcocite precipitates heated during x-ray analysis showed diffraction evidence of $CuSO_4 \cdot 5H_2O$ production.

In support of the model discussed above, Fig. 5 shows that an area of predominantly djurleite can be converted to a region consisting mainly of chalcocite and voids. As the mixture of chalcocite and djurleite was heated above 150°C, the

bonding of excess sulfur with oxygen became favorable to the hexagonal-to-cubic conversion. Thus a compound such as $CuSO_4$ with a sulfur to copper ratio greater than 1:2 was probably produced, resulting in a net sulfur loss. Pits then began to form at reaction sites where the copper sulfide was breaking down and bonding with oxygen. The excess copper from the cupric sulfate reaction,

$$Cu_{2-x}S + 2O_2(g) \underset{0<x<0.6}{\longrightarrow} CuSO_4 + (1-x)\,Cu(m) \ ,$$

then entered the copper deficient $Cu_{2-x}S$ surrounding the reaction pits. The resulting microstructure after cooling consisted of reaction voids surrounded predominantly by chalcocite.

The final location of the $CuSO_4$ reaction product is not clear although it should be noted that $CuSO_4$ begins to dissolve at 200°C and is soluble in water.[35]

For temperatures below 100°C, the h.c.p.-c.c.p. activation barrier is not encountered, so the dominant reaction with air probably involves the copper atoms alone. ($CuSO_4$ formation has not been observed for $T < 100$°C.) A further distinction between oxidation modes is that sulfur oxidation requires the dissolution of the copper sulfide structure, whereas copper oxidation requires the diffusion of the highly mobile copper atoms[36] to the surface, without major disruption of the sulfur sublattice. Thus, one would expect sulfur oxidation to occur at specific reaction sites where sulfur atoms could be removed with a minimum number of broken bonds. Conversely, copper oxidation probably occurs uniformly on the surface of the copper sulfide. Heating a copper sulfide layer above 150°C after an oxidizing treatment below 100°C would therefore have a different effect than a heat treatment without a previous low-temperature oxidation step. A copper oxide or copper carbonate layer on the surface, produced by low-temperature exposure to air, would prevent sulfur from making contact with the free oxygen during the subsequent heat

treatment above 150°C. Formation of Cu-S-O compounds such as $CuSO_4$ would thus be inhibited.

Fig. 7 illustrates such a case. The pre-treatment oxidation created a passifying layer of copper oxide (or copper carbonate) on the specimen surface. The observed effect of the short heat treatment at 180°C was probably due to the clustering of copper vacancies which were formed during pre-treatment (see Part B of the Discussion). Cooling resulted in a microstructure of djurleite with a copper oxide or carbonate coating (Fig. 7b). If the model described in this section is fundamentally correct, then the extended contact of air with $Cu_{2-x}S$ should be avoided between conversion and heat treatment.

The following properties of this model are relevant to the understanding of heat treatments in air given to $Cu_{2-x}S$/CdS solar cells:

i. Oxidation of copper results in a layer of copper oxide (or carbonate) on the surface of the $Cu_{2-x}S$ whereas oxidation of sulfur (or the formation of $CuSO_4$) occurs in localized reaction sites.

ii. For $T < 100°C$, oxidation of copper produces a thin layer of copper oxide (or carbonate) on the $Cu_{2-x}S$ surface which inhibits the formation of $CuSO_4$, thereby preventing copper enrichment of the $Cu_{2-x}S$ layer during subsequent heat treatments above 150°C.

iii. In the range $100 < T < 150°C$, conversion to the metastable tetragonal phase ($\sim Cu_{1.96}S$) is preferable to the transformation to a hexagonal chalcocite-cubic digenite mixture, thus oxidation of copper remains dominant.

iv. For $150°C < T < T_{max}$ (where T_{max} is the approximate temperature at which the hexagonal-cubic transformation occurs, the large activation barrier of the hexagonal-cubic transformation encourages the oxidation of excess sulfur to form a compound such as $CuSO_4$, thereby increasing the copper-to-sulfur ratio of the remaining copper sulfide. During extended heat treatments

in this temperature range, a surface layer of copper oxide is eventually formed. This surface layer prevents free oxygen from contacting sulfur, and $CuSO_4$ production is terminated. Thus, oxidation beyond this point can no longer increase the copper-to-sulfur ratio in $Cu_{2-x}S$. Instead, the surface copper is depleted further, resulting in the djurleite structure upon cooling.

v. Above T_{max}, the equilibrium mixture of hexagonal chalcocite and cubic digenite is easily established. Consequently, oxidation of sulfur by the mechanism outlined in (iv.) does not occur.

While the results shown in Figs. 5 through 7 support the model described above, they represent the only two sequences obtained thus far. A matrix of sequences with varying heat treatment atmospheres (e.g. O_2, CO_2, H_2O), temperatures, and starting compositions will be needed to fully substantiate the interpretations presented in this section. In addition, a measurement of the hexagonal chalcocite to cubic digenite activation energy, possibly by hot stage in situ TEM, will be helpful in estimating T_{max}.

B. The Structures of Chalcocite and Djurleite.

Using the atom positions reported by Evans[28,29], the structures of chalcocite and djurleite can be compared as follows:

1. Chalcocite (Cu_2S).

The chalcocite structure has a well-developed $Cu_{12}S_6$ repeat unit (see Fig. 13). The pseudo-orthorhombic unit cell contains 16 of these units. All have approximately the same structure although exact atom positions vary from one unit to the next. The prominent feature of these $Cu_{12}S_6$ groups is a ring of five copper atoms occupying five corners of a distorted hexagon. The spacial arrangement of these building units is indicated in Fig. 14.

2. Djurleite ($Cu_{1.938}S$).

Examination of the djurleite structure did not reveal a repeating building unit which involves all of the atoms of the unit cell. However, "double building units" of composition $Cu_{20}S_{12}$ are located at body-centered sites of the pseudo-orthorhombic unit cell. These clusters resemble two chalcocite building units placed base-to-base. The major difference is that the two five-member rings are replaced by a single six-member ring (see Fig. 15). The remaining copper atoms in the unit cell are ordered in a manner similar to the ordering of copper in chalcocite.

The two $Cu_{20}S_{12}$ groups per unit cell account for all eight of the vacancies in a unit cell of djurleite ($Cu_{1.938}S$). The tendency for four vacancies to cluster into a $Cu_{20}S_{12}$ group and the fact that the lattice parameters of $Cu_{1.969}S$ and $Cu_{1.938}S$ are similar, lead to the conclusion that there is probably no radical difference between the structures of these two forms of djurleite. Therefore, it seems likely that the four vacancies per unit cell of $Cu_{1.969}S$ are all clustered into one $Cu_{20}S_{12}$ group with the remainder of the copper atoms ordered in groups similar to the building units of chalcocite.

3. Model of the Chalcocite to Djurleite Transformation

Based upon the observations of the above sections, the following model of the low temperature oxidation of chalcocite to djurleite has emerged:

First, the relatively well-ordered chalcocite loses some copper to oxygen or CO_2 at a free surface or grain boundary. The high mobility of copper allows groups of four Cu vacancies to readily cluster into $Cu_{20}S_{12}$ units. These clusters assume their lowest energy by ordering in an orthorhombic fashion with copper and sulfur atoms appearing in a two-to-one ratio surrounding the $Cu_{20}S_{12}$ groups. The resulting interface is between chalcocite and djurleite ($Cu_{1.969}S$).

Further copper removal at the chalcocite/djurleite boundary leads to the motion of this interface and the clustering of more copper vacancies into $Cu_{20}S_{12}$

groups. These additional clusters form at sites in body-centered positions of the unit cells of djurleite. A region saturated with these clusters has 8 copper vacancies per unit cell volume and a composition of $Cu_{1.938}S$, which is the composition of the djurleite studied by Evans[28]. Thus, djurleite may be regarded as a solid solution with a constant orthorhombic framework of $Cu_{20}S_{12}$ groups. Compositions between $Cu_{1.938}S$ and $Cu_{1.969}S$ can be achieved by a statistical distribution of $Cu_{20}S_{12}$ clusters among the body-centered sites. Copper loss from $Cu_{1.938}S$ results in the formation of phases which are beyond the scope of this investigation.

The following points are of primary interest:

i. The chalcocite building unit is the fundamental configuration of copper and sulfur in both structures.

ii. Djurleite is based on an ordered framework of $Cu_{20}S_{12}$ units which result from the clustering of copper vacancies.

iii. The solid solution character of djurleite can be explained by the accommodation of a second $Cu_{20}S_{12}$ (4 vacancy) cluster in the body-centered site of the $Cu_{1.969}S$ unit cell (corresponding to the $Cu_{1.938}S$ structure determined by Evans[28]). The copper and sulfur atoms not in $Cu_{20}S_{12}$ clusters are distributed about the clusters in a two-to-one ratio with ordering similar to that of chalcocite.

iv. The high mobility of copper ions, the propensity for copper vacancies to cluster, and the very slight lattice mismatch between chalcocite and djurleite, lead to sharp coherent interfaces between the two phases (see Figs. 8 through 12). The rate of interface motion may be determined by the rate of copper diffusion to the surface along interfacial diffusion paths.

C. Chalcocite/Djurleite Interfaces.

In addition to yielding information regarding the effects of air on $Cu_{2-x}S$, the technique of high resolution electron microscopy allows direct observation of chalcocite/djurleite interfaces. Fig. 16 schematically illustrates ten variations of vertical chalcocite/djurleite interfaces (containing the c-axis). Each of the interfaces observed in this study fits into one of these ten categories. The number below each diagram is the percent misfit in the sulfur basal plane calculated with the data reported by Evans for $Cu_{2.000}S$ and $Cu_{1.938}S$[28,29] (the chalcocite sublattice is always larger than the djurleite sublattice).

Based on a reduction of strain energy alone, one would expect to observe mostly E (0.1%) or G (0.3%) interfaces. Accordingly, the most common interface observed in this study was E (Figs. 8, 9, and 11) followed by G (Figs. 8 and 11). Close examination of Fig. 8 reveals an E,G interface which appears to be very coherent and essentially strain free. A lower magnification image of the same region (Fig. 5a) shows that this interface is roughly flat for at least 1000Å, considerably longer than any other chalcocite/djurleite boundary imaged in this study.

As expected, the higher mismatch interfaces (F: 1.0% and H: 1.2%) were observed infrequently and found to be short (~60Å) and highly strained (see Fig. 9). Correspondingly, the 0.6 to 0.7% mismatch interfaces imaged in Figs. 10 (B) and 12 (A and D) are intermediate in length (100 to 200Å).

Note that the low strain E,G interface imaged in Figs. 11 and 5b has apparently swept across the area of interest in the 4 days between Figs. 5b and 5c. Thus, preliminary indications are that the low temperature chalcocite-to-djurleite transformation proceeds by the motion of low strain interfaces (such as E and G) at the expense of higher strain regions (such as the island of djurleite imaged in Fig. 5b).

Further observations of chalcocite/djurleite interfaces, including measurement

of the dependence of growth rate on interface orientation and environment, should lead to a more complete understanding of the chalcocite-to-djurleite degradation mechanism at temperatures below 100°C (including the operating range of $Cu_{2-x}S$/CdS solar cells). However, before observations of these interfaces can be properly interpreted, the nature of the faulting observed on (040) planes of chalcocite (Figs. 8, 11, and 12) must be clearly understood.

D. Faulting in Chalcocite.

The frequently observed variation in spacing along the [010] direction in chalcocite is most easily explained by the 1/4 [010] fault diagrammed in Fig. 17. The 5-Cu layers of the $Cu_{12}S_6$ building unit are represented as in Fig. 14. Note that, in the unfaulted structure, a copper atom is associated with each side of the hexagon. Therefore, each hexagon contains 4 + 1/2 + 1/2, or five, copper atoms. If this same rule is obeyed for the faulted structure in Fig. 17, then each hexagon along the fault contains an average of four copper atoms. Thus, the densely-packed copper layers along the fault are likely sites for copper vacancies (and possibly Cd^{++} impurities).

Further support for this model comes from the observation of these faults near chalcocite/djurleite interfaces. Vacancy condensation along these faults would slightly reduce the average S-S distance in the basal plane, thereby affording a better lattice match with djurleite. However, if the 5-Cu layers remained intact at the fault, the resulting expansive strain on the sulfur sublattice would increase the lattice mismatch between chalcocite and djurleite. Therefore, it seems spatially and energetically favorable for vacancies to condense on these chalcocite 1/4 [010] faults. In fact, comparison of faulted regions with adjacent unfaulted areas show that the fault width is approximately 8% smaller than the separation between (040) planes in unfaulted chalcocite (for example, lattice parameter measurements of the area imaged in Fig. 11 show that the fault width is 6.3 ± 0.3Å compared to the unfaulted (040) separation of approximately 6.8Å).

Perhaps the most interesting consequence of this model is the predicted variation in the copper-to-sulfur ratio allowed by these faults. Table 1 shows the calculated composition of chalcocite as a function of the average distance between faults along with the percent lattice contraction assuming an 0.5Å contraction per fault.

TABLE 1

CALCULATED COMPOSITIONS OF FAULTED CHALCOCITE

Spacing between faults in [010] direction	Lattice contraction in [010] direction	Composition (2-x)
34Å	1.5%	1.933
48	1.1	1.952
61	0.8	1.963
75	0.7	1.969
89	0.6	1.974
102	0.5	1.978
143	0.3	1.984
280	0.2	1.992
1000	-	1.996

Note that a fault spacing of 75Å (equivalent to five 13.6Å wide unfaulted layers separating each 6.3Å wide faulted layer) yields a composition of $Cu_{1.969}S$, the copper-rich end of the djurleite solid solution range. This may explain the unexpected results obtained by Putnis (described in the Introduction)[26].

The verification of this model with further microscopy, including careful lattice parameter measurements, may allow the association of compositional maps with high resolution images of chalcocite. Such maps would be very useful for quantifying the effects of environment on copper sulfide.

V. CONCLUSION

This study represents the first real space observation, to the author's knowledge, of the chalcocite-djurleite microstructure. Consequently, as many questions were raised as were answered. The following is a brief summary of the two models developed here, along with suggestions for future work that may be necessary to substantiate each model.

A. The Heat Treatment Model: T > 100°C.

The results presented in Figs. 5 through 7 suggest that a beneficial effect of the standard air heat treatment at 150 to 250°C of $Cu_{2-x}S$/CdS solar cells may be the net increase in the copper-to-sulfur ratio of the $Cu_{2-x}S$ layer. This effect is due primarily to the large activation barrier encountered in the hexagonal chalcocite to cubic digenite transformation. During heat treatment in air above 150°C, the activation barrier is avoided when excess sulfur bonds with oxygen and copper to form a compound such as $CuSO_4$, thereby increasing the Cu:S ratio of the remaining copper sulfide. The production of $CuSO_4$ at localized reaction sites is eventually slowed by a thickening layer of copper oxide which forms uniformly on the surface, preventing contact between excess sulfur and free oxygen.

At temperatures between approximately 100 and 150°C, the formation of the metastable tetragonal phase eliminates the need to release excess sulfur. Sulfur rich compositions are also accommodated at temperatures substantially above 150°C for which the hexagonal-to-cubic transformation proceeds with ease. Thus, sulfur loss by the activation barrier mechanism occurs only in the window of temperatures between 150°C and a higher temperature T_{max} (which depends slightly on the

duration of the heat treatment). T_{max} may be determined by measurements of the activation barrier in an in situ hot-stage electron microscope. Verification and refinement of this model may be achieved by gathering a matrix of high resolution data such as that presented in Figs. 5 through 7.

B. The Stoichiometry/Structure Model: $T < 100°C$.

The ordering of copper in chalcocite and djurleite is shown to be similar. The major distinction is the condensation of groups of four vacancies to form the $Cu_{20}S_{12}$ units of djurleite. Ordering of these four-vacancy units results in the solid solution character of djurleite with (2-x) varying from 1.969 (4 vacancies per unit cell) to 1.938 (8 vacancies per unit cell).

The fairly regular arrangement of $Cu_{12}S_6$ building units in chalcocite is occasionally interrupted with 1/4 [010] faults. Spacial requirements indicate that these faults are likely locations for vacancy condensation. According to this model, a fault spacing of approximately 75Å results in a composition with (2-x) = 1.97, the copper-rich composition of the djurleite solid solution range. This model may be substantiated by further high resolution electron microscopy. It will then be possible to directly correlate a high resolution image of copper sulfide with a compositional map, thereby allowing a more quantitative description of the effects of environment on copper sulfide.

Preliminary results indicate that the low temperature chalcocite-djurleite transformation proceeds by the motion of low-strain coherent interfaces. Diffusion of copper to the surface along interfacial diffusion paths may be the rate-determining mechanism. However, observations of interface motion in various atmospheres (e.g. O_2, CO_2, and H_2O) will be needed to test this hypothesis.

Continuing refinement of these two microstructural models may lead to a thorough understanding of the $Cu_{2-x}S$-air interaction; an understanding which is

necessary for the logical development of reproducible, efficient, and stable solar cells containing copper sulfide.

ACKNOWLEDGEMENTS

I would like to thank my advisors, Professor Jack Washburn and Dr. Ronald Gronsky, for their innovative suggestions and practical guidance throughout the course of this work. Special thanks also go to my "adopted advisor", Dr. Ulrich Dahmen, for many helpful discussions in the early stages of this study.

I greatly appreciate the assistance of Madeline Moore in preparing the manuscript. It was a pleasure to work with her and the other members of the Lawrence Berkeley Laboratory and University of California, Berkeley staffs.

Finally, I would like to express my gratitude for the encouragement and support provided by my family, friends and especially my wife, Laura.

This work was supported by the Director, Office of Energy Research, Office of Basic Energy Sciences, Division of Materials Sciences of the U. S. Department of Energy under Contract No. W-7405-ENG-48.

Appendix

Phase Contrast Electron Microscopy of Copper Sulfide

Background

The charged nature of the electron and its small deBroglie wavelength (0.037 Å at 100 keV) can be utilized in modern transmission electron microscopes (TEM) to probe solids at the atomic level. In the evacuated column of a TEM, a nearly monochromatic beam of energetic (100keV to ~3 MeV) electrons is manipulated by Lorentz forces from high precision magnetic lenses. The interaction of these electrons with a suitably thinned crystalline specimen can be described by the dynamical theory of electron diffraction. Fortunately, a more intuitive description (the kinematical approach) yields the principle geometric results.

One must first imagine a three-dimensional space described by vectors which are normal to the real space atomic planes. The length of each vector is the reciprocal of the distance between the corresponding atomic planes. This space is termed reciprocal or Fourier space. The reciprocal lattice vectors are usually denoted by $\vec{g}_{hkl}$ where h, k, and l are the Miller indices of the atomic planes.

Simple scattering theory (see Kittel[37] for details) shows that the scattered amplitude is proportional to the volume integral over the Fourier coefficients of the electron density (in the crystal) multiplied by $\exp[i[(\vec{g} - \Delta\vec{k}) \cdot \vec{r}]]$ (where $\Delta\vec{k}$ is the vector difference between the incident and scattered wavevectors). This integral is negligible except for scattered $\vec{k}$ vectors which satisfy $\Delta\vec{k} = \vec{g}$. thus, for elastic scattering, we have the following condition:

$$(\vec{k} + \vec{g}) = |\vec{k}|^2 .$$

This equation describes a sphere of radius $|\vec{k}|$ (Ewald sphere) passing through the origin of reciprocal space. The vector extending from the center of the sphere to

the origin of reciprocal space is the incident wavevector $\vec{k}$. Those reciprocal lattice points which lie on this sphere represent the possible diffracted beams of non-zero amplitude. (Note that reciprocal lattice points have finite extent so they need not lie exactly on the sphere in order to contribute non-zero amplitude.)

Since the radius of this sphere is proportional to $1/\lambda$, the small wavelength of TEM electrons results in a large Ewald sphere. If oriented tangent to a reciprocal lattice plane, the Ewald sphere's intersection with the reciprocal lattice is nearly planar. The characteristic two-dimensional electron diffraction pattern results (for example, see Fig. 4).

The same diffraction pattern can be rationalized by beginning instead with the familiar expression for Braggs Law, $\lambda = 2d \sin \theta$. Consider the atomic planes of the crystal to be parallel reflecting planes. For d on the order of several angstroms and $\lambda \tilde{=} 0.04$ Å (100 keV electrons), one obtains a Bragg angle of less than a degree. Therefore, all sets of reflecting planes with their normals approximately 90° to the incident direction, will produce a diffracted beam. When recorded on a two-dimensional plane perpendicular to the incident direction, the distance between each diffracted spot and the forward scattered spot will be proportional to the reciprocal of the corresponding atomic plane spacing.

To summarize, an electron diffraction pattern is a nearly one-to-one map of a plane in reciprocal space. The vector from the origin (forward scattered spot) to each diffracted spot can be regarded as a reciprocal lattice vector $\vec{g}_{hkl}$ ($|\vec{g}_{hkl}| = 1/d_{hkl}$) representing diffraction from the (hkl) planes. The intensity of each spot is determined primarily by accelerating voltage, specimen thickness, orientation, and structure factor. Further geometric information can be extracted from the diffraction pattern by recognizing the reciprocal relationship between the shape of the reciprocal lattice point and the geometry of the specimen.[38]

To obtain the real space image corresponding to this diffraction pattern, one

must recombine the diffracted beams and magnify the result. With ideal optics (no spherical aberration), one would expect to see a real space image of the specimen with all spatial periodicities reproduced. Unfortunately, electron optics are not ideal and we must make some compromises.

Practical Considerations

Spherical aberration (C_s) and objective lens defocus (D) combine to create an undesirable phase shift of the diffracted beams relative to the forward scattered beam. The magnitude of this phase shift as a function of α, the angle between the diffracted beam and the forward scattered beam, is

$$X(\alpha) = \frac{\pi}{\lambda}\left(\frac{C_s\alpha^4}{2} + D\alpha^2\right) . \quad 39$$

The function $e^{iX(g)}$ ($g = \alpha/\lambda$) is known as the contrast transfer function (CTF). In practice, the CTF can be optimized by imaging in an underfocused condition (the Scherzer defocus)

$$D \cong -(C_s\lambda)^{1/2} \quad 40 .$$

To guarantee an image with optimum defocus, one always records a through-focal series.

Even at optimum underfocus, contrast transfer is generally poor for diffracted beams with high values of $|\vec{g}|$. When recombined with the forward scattered component, these high $|\vec{g}|$ diffracted beams increase the background noise, thereby reducing the overall image contrast. To remove these spurious signals, the electron microscopist may insert an objective aperture at the back focal plane. An aperture of the proper size will allow only those beams with acceptable contrast transfer characteristics to recombine with the forward scattered beam.

Therefore, one can vary the defocus and the objective aperture size to obtain the optimum compromise between the quantity of information (number of diffracted beams admitted) and quality of information (contrast). However, to recognize a truly representative structure image, one must resort to dynamical theory calculations (including thickness effects).

Applications to $Cu_{2-x}S$

The shadow of the objective aperture used for this study is imaged in Fig. 4a. This aperture does not yield the maximum possible resolution (since no direct information from the sulfur sublattice is transferred to the image). However, the small size of the aperture is an advantage when image contrast is considered. The reduced effect of spherical aberration allows the image to be clearly seen on the phosphorescent screen at a magnification of 250kX (especially for chalcocite). This visibility, in turn, assures that the image can be adjusted and recorded with a minimum of exposure to the electron beam.

Sequential images of the same region of $Cu_{2-x}S$ were obtained by following the procedure outlined below:

1. The specimen was inserted into the Siemens 102 double-tilt specimen holder. A marker on the specimen support ring indicated the position of the specimen within the holder.
2. After the microscope alignment was checked, the specimen and holder were mounted in the column (100kV operating voltage).
3. A thin area of proper orientation was located by translating and tilting at low magnification (50kX). All parameters including tilt angles, translator positions, and specimen height were recorded.
4. The highest possible symmetry of the diffraction pattern was obtained by careful tilting. The objective aperture was inserted and centered.

5. At 100kX, the objective astigmatism was adjusted until the Fresnel fringes around a hole or curved edge appeared even in thickness.
6. The magnification was increased to its final value of between 250kX and 400kX. The level of illumination was set with the condenser lens and the centering of the objective aperture was re-checked in the diffraction mode.
7. The objective astigmatism was adjusted until non-directional fine-grain contrast could be observed in the amorphous region at the specimen edge. At this point lattice fringes were usually visible.
8. The defocus was set to approximately zero by varying the fine focus of the objective lens until a focal point of minimum contrast and maximum definition was observed.
9. A through-focal series was recorded by photographing images at incremental amounts of negative defocus.
10. The specimen was removed and subjected to the desired treatment in air. the procedure described above was repeated with the identical area by adjusting all microscope parameters to the values recorded for the first through-focal series. However, minor adjustments were frequently necessary.

REFERENCES

1. J. Leong and S. Deb, SERI/TP-613-1220 (1981).
2. K. W. Böer, phys. stat. sol. (a) 19, 13 (1978).
3. R. H. Bube, "Solar Cells" in Handbook on Semiconductors, vol., 4: Device Physics, Editors: T. S. Moss and C. Hilsum (North Holland, 1981), 691.
4. H. J. Hovel, "Solar Cells" in Semiconductors and Semimetals, vol. 11, Editors: R. K. Willardson and A. C. Beer (Academic Press, 1975).
5. R. Hill, Solid-State and Electron Dev. 2, S49 (1978).
6. S. Salkalachen et al., Solar Cells 3, 341 (1981).
7. J. Washburn and T. Peterson, phys. stat. sol. (a) 22, 721 (1974).
8. N. Convers Wyeth and A. W. Catalano, 12th IEEE Photovoltaic Spec. Conf., 471 (1976).
9. B. G. Caswell, G. J. Russell and J. Woods, J. Phys. D: Appl. Phys. 8, 1889 (1975).
10. F. Pfisterer, G. H. Hewig, and W. H. Bloss, 11th IEEE Photovoltaic Spec. Conf., 460 (1975).
11. F. Pfisterer, H. W. Schock, and W. H. Bloss, 11th IEEE Photovoltaic Spec. Conf., 502 (1976).
12. F. Arjona et al., 12th IEEE Photovoltaic Spec. Conf., 515 (1976).
13. A. W. Czanderna, E. T. Prince and H. F. Helbig, Proceedings of SPIE 248, 74 (1980).
14. J. J. Loferski et al., 12th IEEE Photovoltaic Spec. Conf., 496 (1976).
15. L. C. Burton and H. M. Windawi, J. Appl. Phys. 47, 4621 (1976).
16. B. G. Caswell and J. Woods, phys. stat. sol. (a) 44, K47 (1977).
17. K. Bogus and S. Mattes, 9th IEEE Photovoltaic Spec. Conf., 106 (1972).
18. R. J. Mytton et al., 9th IEEE Photovoltaic Spec. Conf., 133 (1972).

19. A. L. Fahrenbruch and R. H. Bube, 10th IEEE Photovoltaic spec. Conf., 85 (1973).

20. W. Palz et al., 10th IEEE Photovoltaic Spec. Conf., 69 (1973).

21. H. M. Windawi, 11th IEEE Photovoltaic Spec. Conf., 464 (1975).

22. H. J. Mathieu, K. K. Reinhartz, and H. Rickert, 10th IEEE Photovoltaic Spec. Conf., 93 (1973).

23. R. W. Potter, Economic Geology 72, 1524 (1977).

24. W. R. Cook, L. Shiozawa, and F. Augustine, J. Appl. Phys. 41, 3058 (1970).

25. E. H. Roseboom, Economic Geology 61, 641 (1966).

26. A. Putnis, Am. Mineralogist 62, 107 (1977).

27. S. Djurle, Acta Chem. Scand. 12, 1415 (1958).

28. H. T. Evans, Science 203, 356 (1979).

29. H. T. Evans, Nature Phys. Science 232, 69 (1971).

30. G. Thomas and M. J. Goringe, Transmission Electron Microscopy of Materials, (John Wiley and Sons, 1979), 27.

31. Some CdS TEM specimens used for this study were prepared by Linda Sindelar, Lawrence Berkeley Laboratory.

32. B. Baron, A. W. Catalano and E. A. Fagen, 13th IEEE Photovoltaic Specialists Conf., 406 (1978).

33. S. Martinuzzi, F. Cabane-Brouty and J. F. Bretzner, 9th IEEE Photovoltaic Specialists Conf., 111 (1972).

34. D. T. Rickard, TMPM Tschermaks Min. Petr. Mitt. 19, 60 (1973).

35. R. C. Weast (Editor), Handbook of Chemistry and Physics, 57th ed. (CRC 1976), B-111.

36. K. Okamoto and S. Kawai, Jap. J. Appl. Phys. 12, 1130 (1972).

37. C. Kittel, Introduction to Solid State Physics, 5th ed. (John Wiley and Sons, 1976), Chap. 2.

38. Reference 30, pp. 80-85.

39. Reference 30, p. 315.

40. O. Scherzer, J. Appl. Phys. 20, 20 (1949).

FIGURE CAPTIONS

Figure 1. Note the deep penetration of copper sulfide down CdS grain boundaries in this schematic cross section. The CdS layer is typically 5 to 30μm thick. $Cu_{2-x}S$ comprises the surface layer to a depth of between 0.1 and 0.3μm. Grain boundary penetrations are usually on the order of 1μm.

Figure 2. The Cu-S phase diagram as determined by Potter[23] is reproduced here for $1.92 < (2-x) < 2.10$. The two-phase region above T = 93°C is composed of cubic digenite (Dg) and disordered hexagonal chalcocite (Ch_{dis}).

Figure 3. The unit cells of djurleite and chalcocite are outlined on the sulfur basal plane in this figure. The dotted line indicates the apparent size of the unit cell of chalcocite in the c-axis projection.

Figure 4. A typical [001] copper sulfide diffraction pattern is indexed here. The chalcocite and djurleite spots are indexed on the left and right, respectively. Of particular interest are the streaks in the chalcocite pattern. In part D of the Discussion, these streaks are shown to be the result of irregularly spaced 1/4 [010] faults. The shadow represents the size of the objective aperture used throughout this study. Note that high resolution images contain no direct information from the sulfur sublattice.

Figure 5. Figure 5a is a high resolution image of an as-plated region of chalcocite and djurleite. The corresponding diffraction pattern is indexed in Figure 4. A similar image of the same area after heat treatment at 180°C for 15 minutes is presented in Figure 5b. Voids are visible in the upper central portion of the picture. The

micrograph in Figure 5c was taken after 4 days in air at 20°C. Further monitoring of this area was prohibited by specimen borne contamination.

Figure 6. The previous figure is mapped out in Figure 6. Note the voids and the apparent increase in the amount of chalcocite in Figure 6b. Figure 6c suggests that the interface just above the crack in 6b has swept across the area of interest to convert the entire region to djurleite.

Figure 7. The effect of low temperature oxidation prior to heat treatment is illustrated in this figure. The djurleite superstructure of Figure 7b has completely replaced the chalcocite ordering apparent in Figure 7a.

Figure 8. This is a high magnification image of the interface in the upper right portion of Figure 5a. Note the high degree of coherency of this low strain E,G interface. The arrow indicates a 1/4 [010] fault in chalcocite.

Figure 9. Two high strain interfaces contribute to the lobes of contrast in Figure 9. An H (1.2%) interface is visible in the lower half of the circle. Slightly lower and to the left is an F (1.0%) interface.

Figure 10. The island of djurleite in Figure 5b is imaged in Figure 10. Both horizontal interfaces are of type B with 0.6% strain.

Figure 11. Another low strain E,G interface is visible in this micrograph (enlarged from Figure 5b). Parts of 1/4 [010] faults are marked with arrows. The upper pair is separated by 34Å while the lower pair is separated by 48Å. Possible consequences of these faults are outlined in part D of the Discussion.

Figure 12. This micrograph shows a reaction site (or void) which is imaged at low magnification in Figure 5b. The arrow points to a 1/4 [010] fault in chalcocite near a type A (0.7%) interface.

Figure 13. An exploded view of the $Cu_{12}S_6$ building unit of chalcocite illustrates the densely packed 5-copper layer. Atom positions are only approximate and vary slightly from one unit to the next.

Figure 14. Successive intermediate copper layers are depicted in this drawing of the chalcocite structure. The 13.6Å periodicity along the [010] direction of chalcocite (for the c-axis projection) is evident.

Figure 15. Four Cu vacancies condense to form this structural component of djurleite. The 5-Cu layer found in chalcocite is shown to be replaced by a 6-Cu layer in this djurleite cluster.

Figure 16. Ten chalcocite/djurleite interfaces are represented here. Wider fringes are the (100) planes of djurleite (16Å spacing). Narrow fringes coincide with the (100) planes of chalcocite (12Å spacing). The number below each diagram is the calculated percent misfit in the sulfur basal plane (the chalcocite sublattice is always larger).

Figure 17. The 1/4 [010] fault of chalcocite is diagrammed here. For simplicity, the fault width is shown as half of the (020) spacing. Measurements indicate that the true fault width is 6.3 ± 0.3Å. As in Figure 14, hexagons represent the densely packed copper layers of the chalcocite building units. Units which have their 5-Cu layers 3.4Å above and below the indicated plane occupy the space between each row of hexagons in Figure 17. One copper atom is associated with each unshared side of a hexagon. Shared sides also contain one copper atom, resulting in the 5-Cu layers of the unfaulted chalcocite and the predicted nonstoichiometry of the faulted chalcocite.

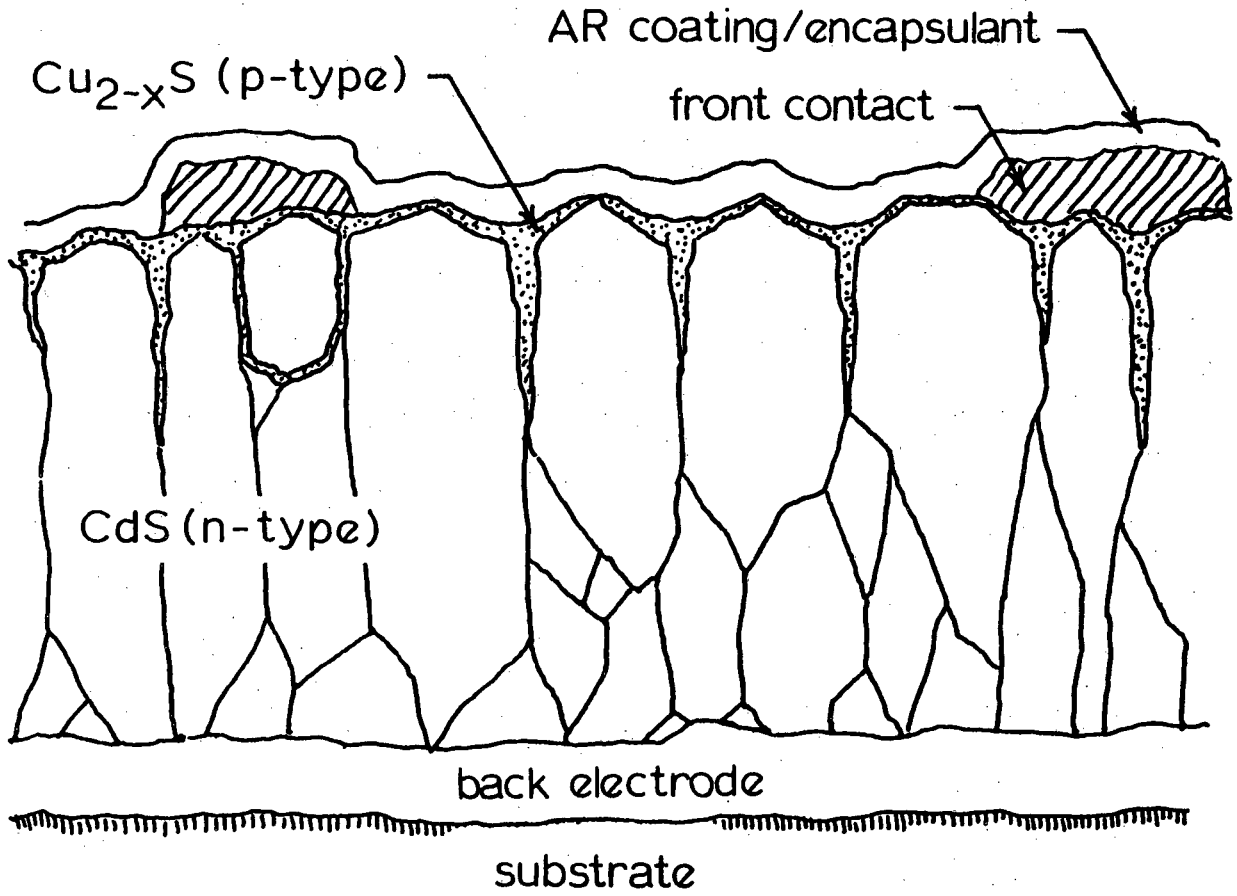

SCHEMATIC CROSS SECTION OF A $Cu_{2-x}S/CdS$ SOLAR CELL

XBL 8110-7085

Fig. 1

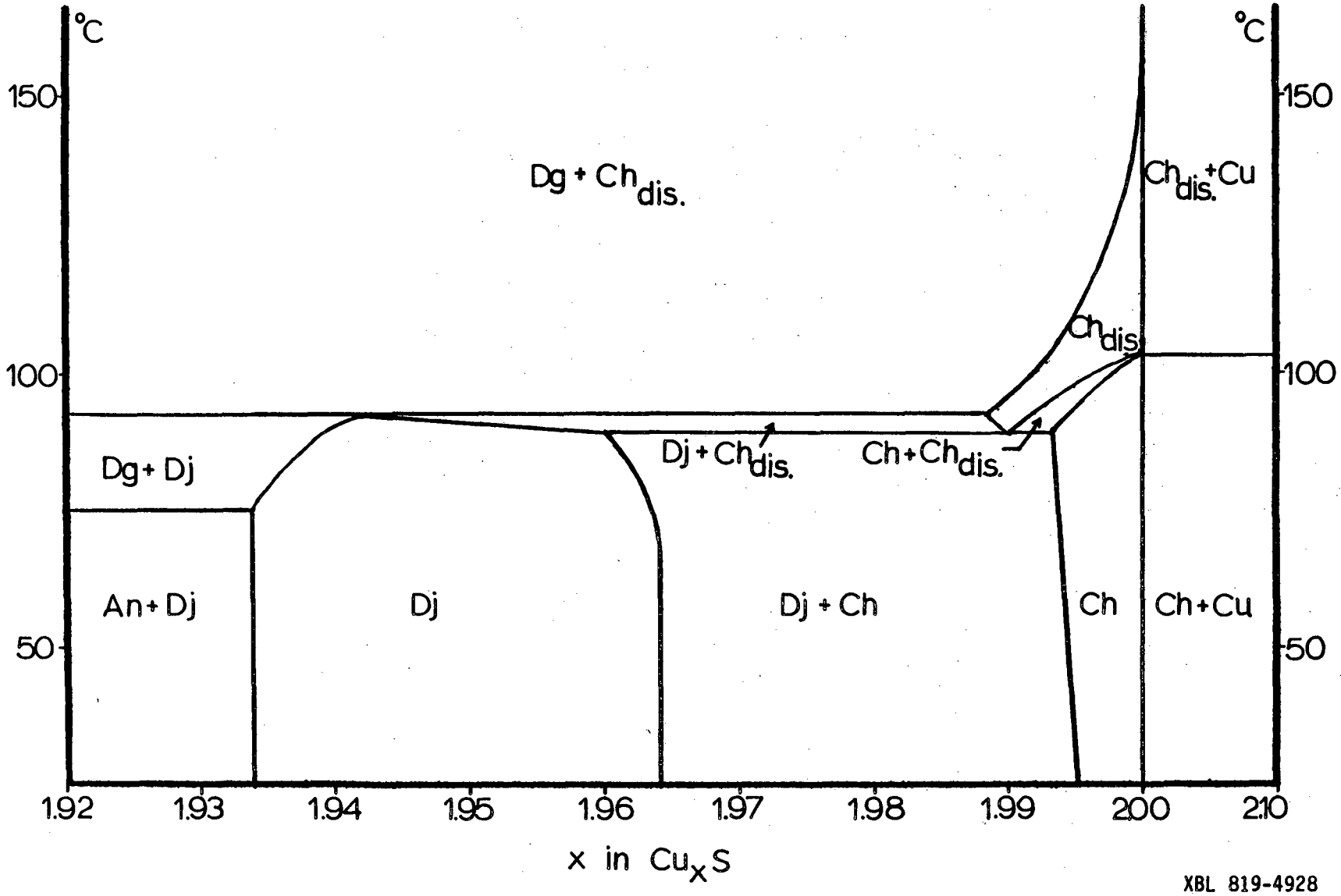
°C
150
100
50
°C
150
100
50
Dg + Ch dis.
Ch dis.+Cu
Ch dis.
Dg + Dj
Dj + Ch dis.
Ch + Ch dis.
An + Dj
Dj
Dj + Ch
Ch
Ch + Cu
1.92
1.93
1.94
1.95
1.96
1.97
1.98
1.99
2.00
2.10
x in Cu x S
XBL 819-4928

Fig. 2

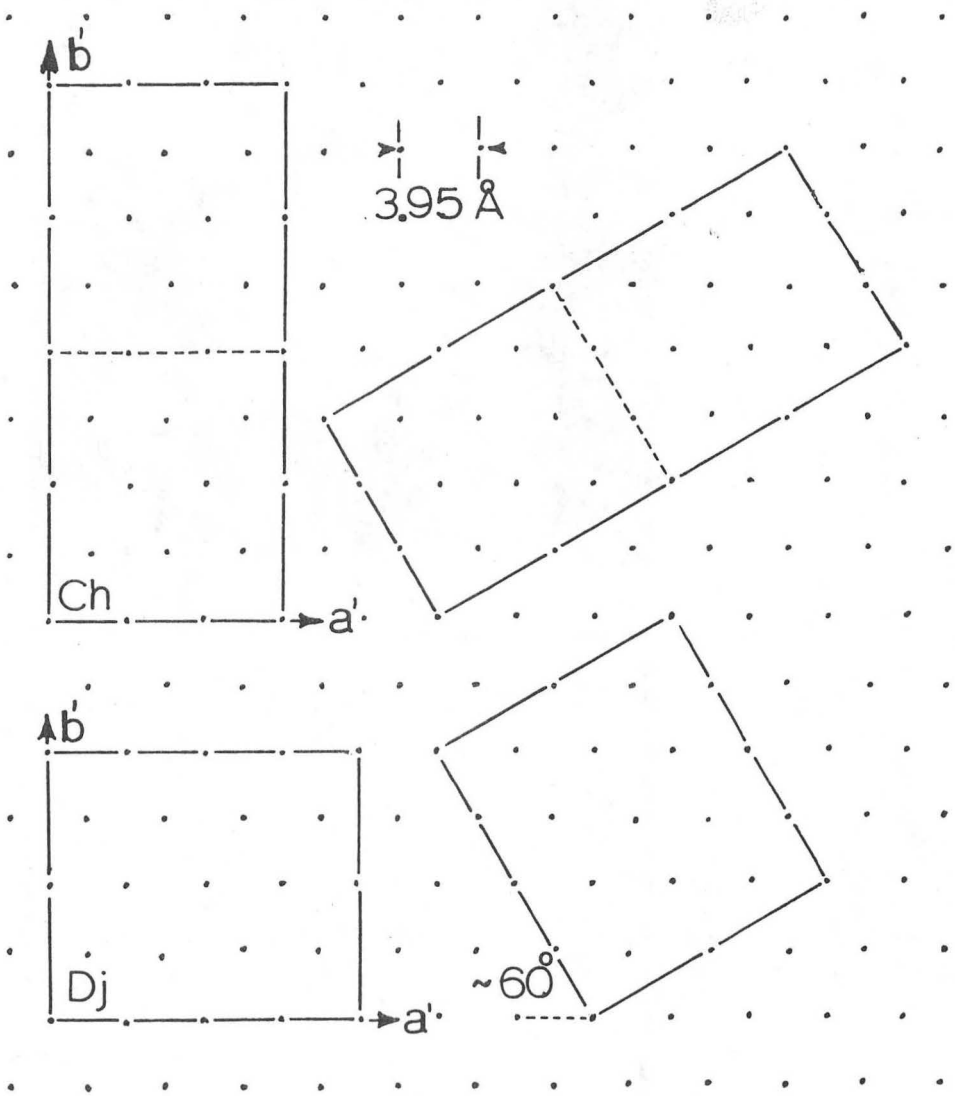

Chalcocite and Djurleite Unit Cells in the Basal Plane of the Sulfur Sublattice

XBL 819-7010

Fig. 3

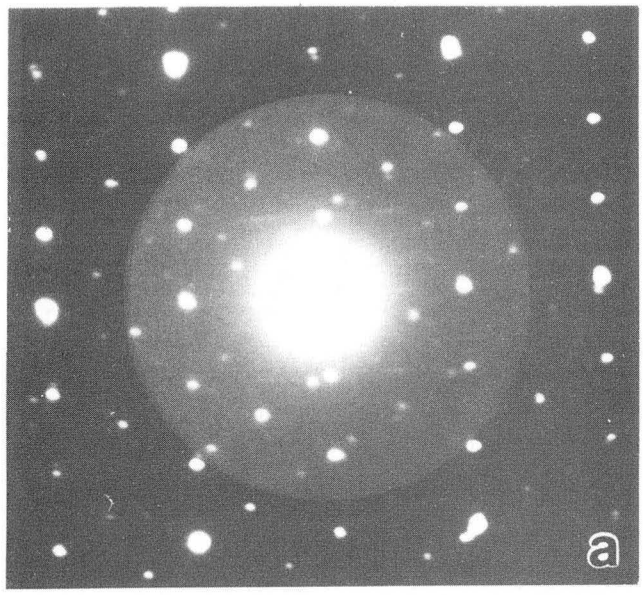

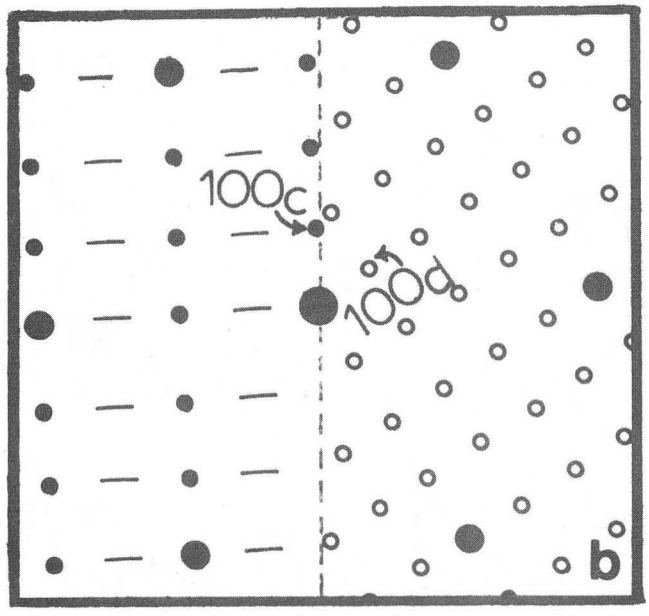

Chalcocite •
Djurleite ○
S sublattice ●

[001]

XBB 8110-9595

Fig. 4

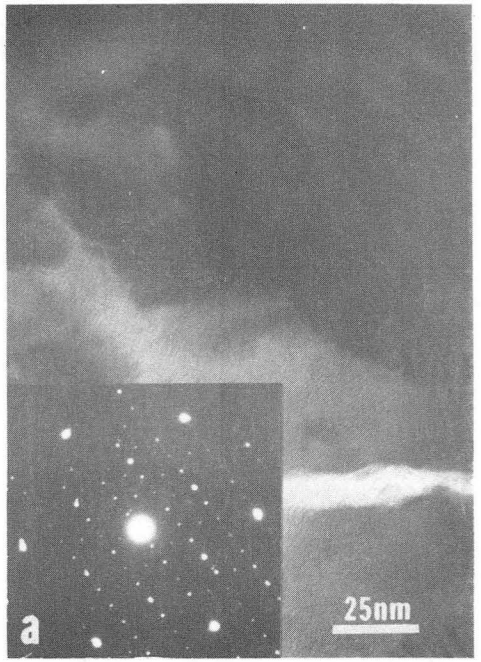

As-Plated

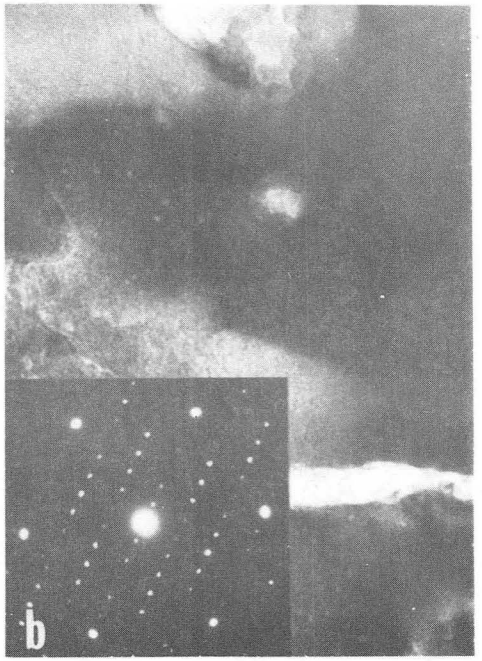

After 15 min. in air at 180°C

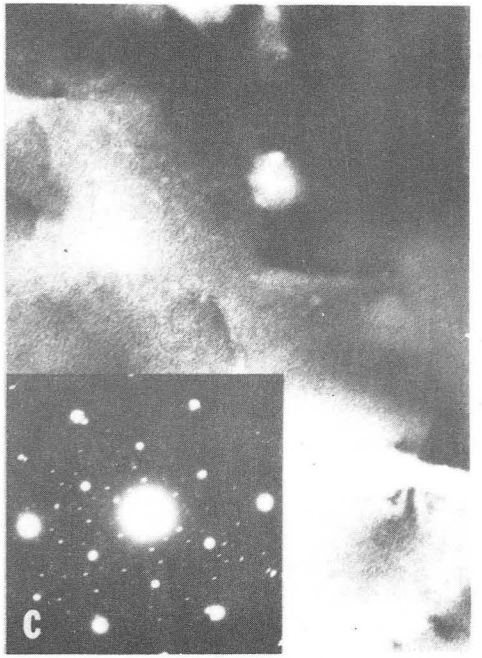

After 4 days in air at 20°C

Fig. 5

XBB 819-8915

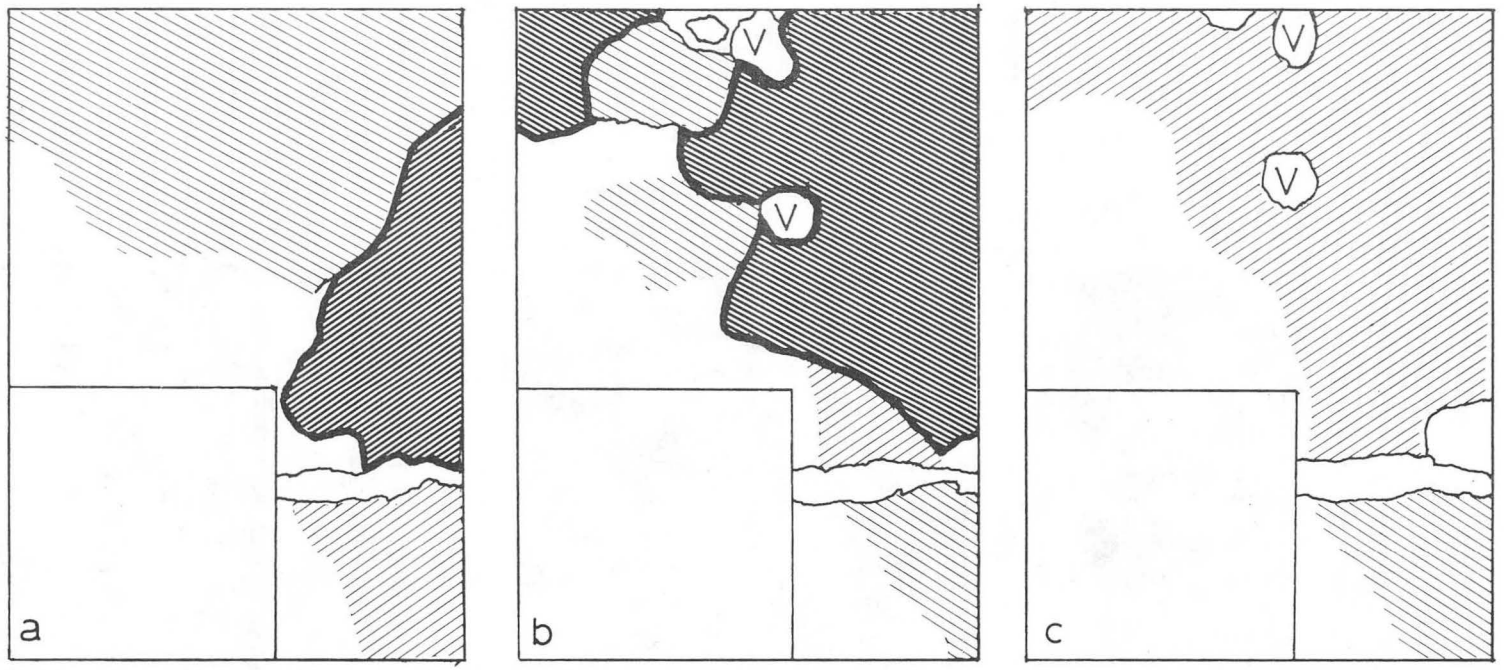

As-Plated

After 15 min. in air at 180°C

After 4 days in air at 20°C

Djurleite

Chalcocite

'a' vectors of pseudo-orthorhombic unit cells are normal to fringes for both phases

Fig. 6

XBL 819-4929

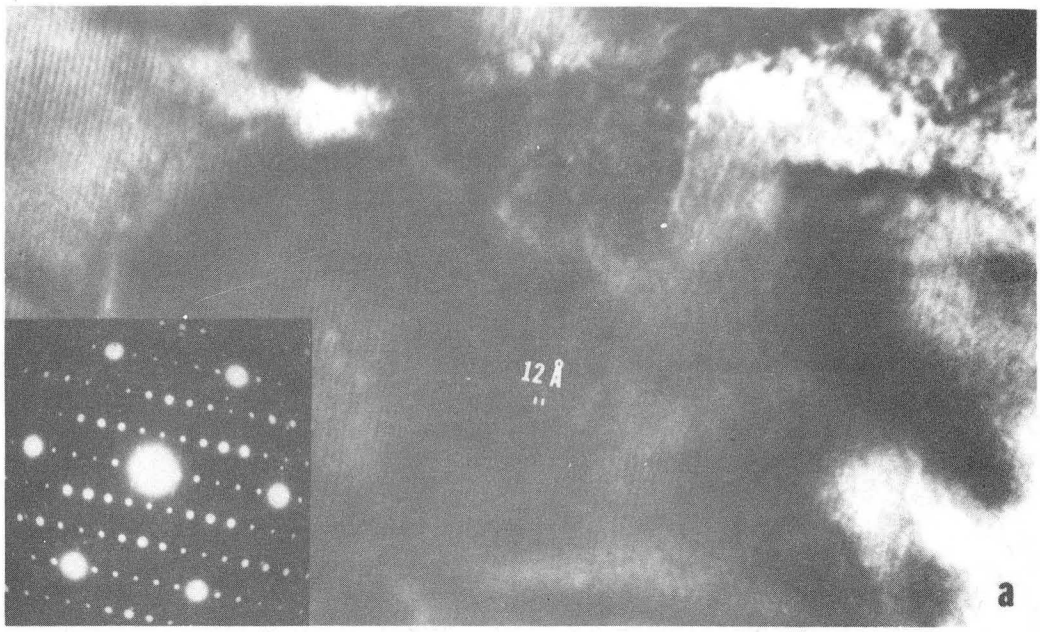

After 20 min. in air at 80° C

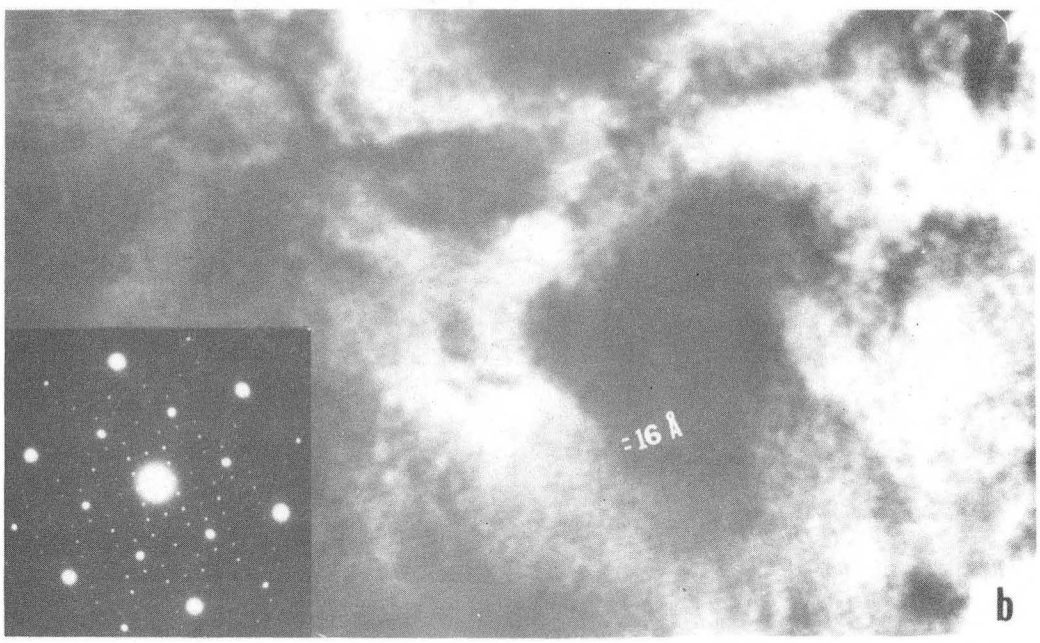

After 5 min. in air at 180°C

XBB 819-8916

Fig. 7

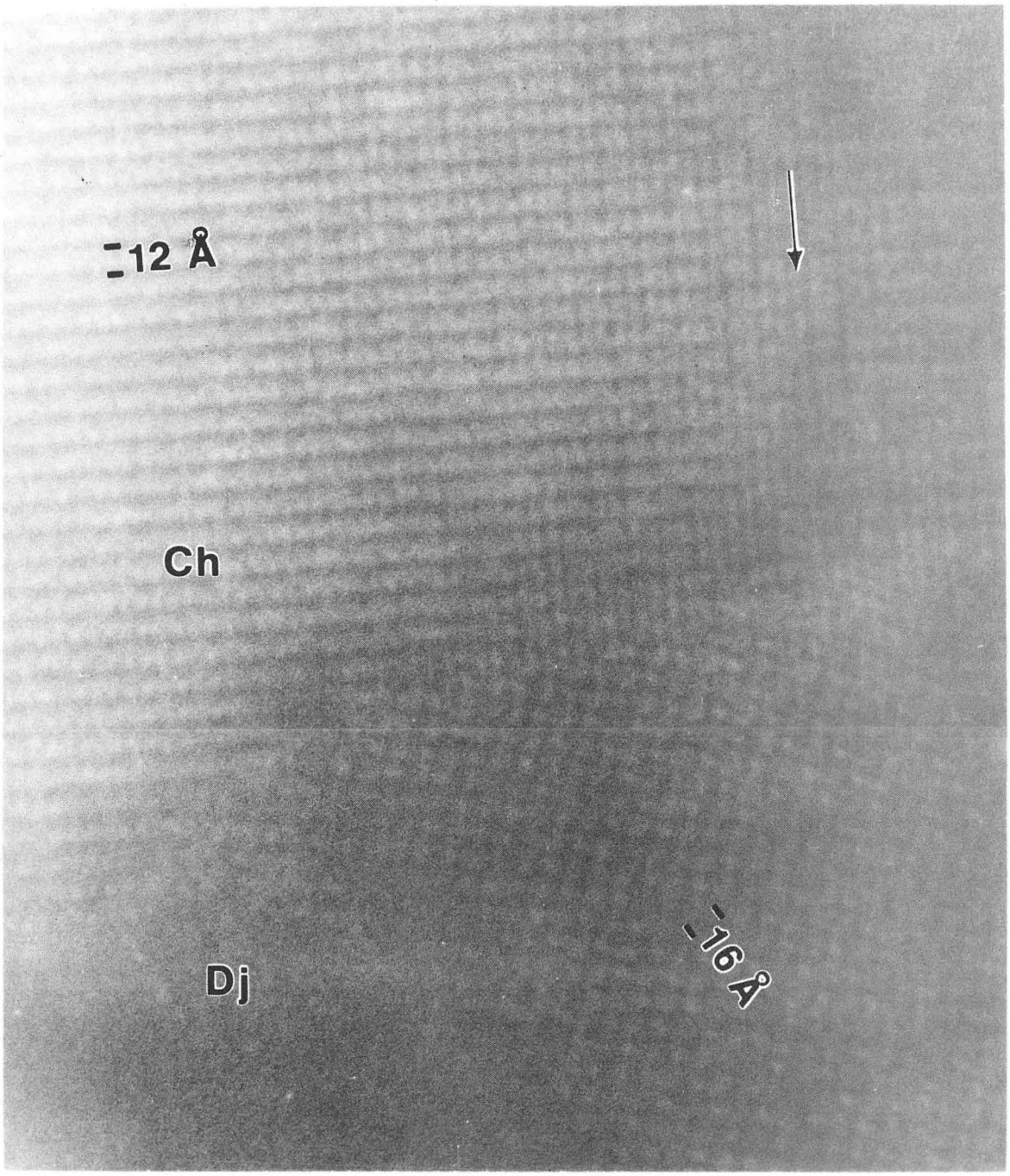

Fig. 8

XBB 8110-9275A

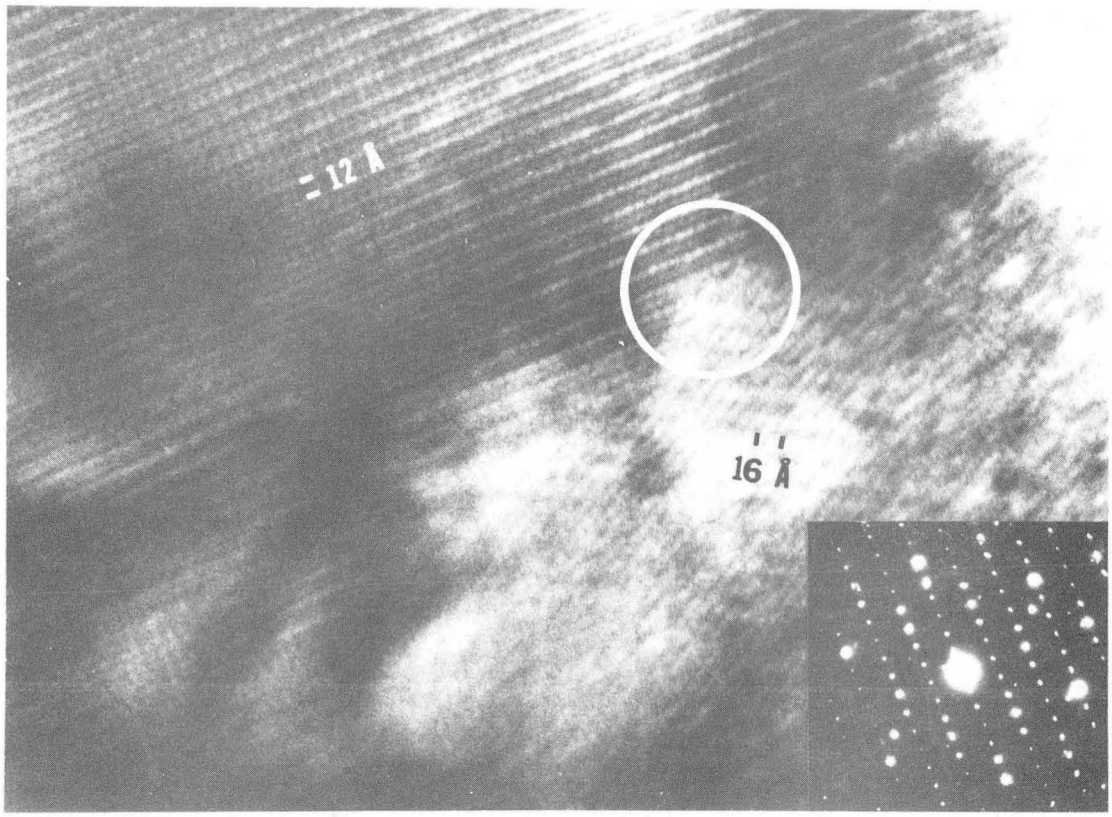

XBB 819-8918

Fig. 9

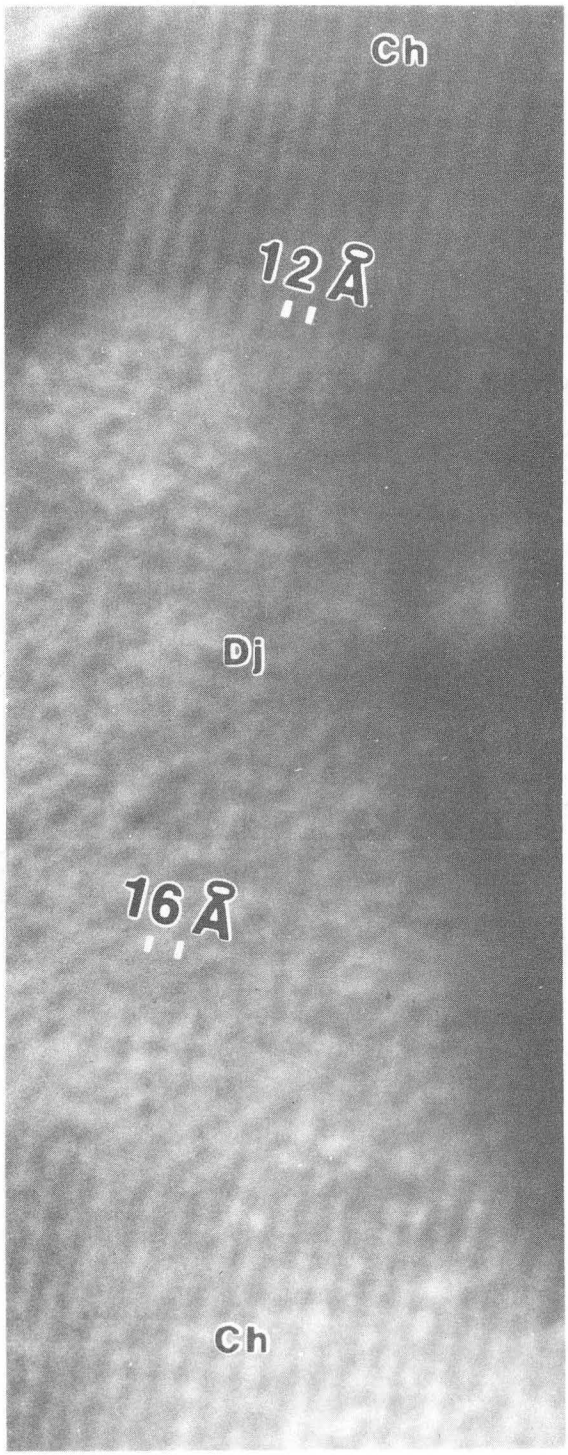

XBB 8110-9595A

Fig. 10

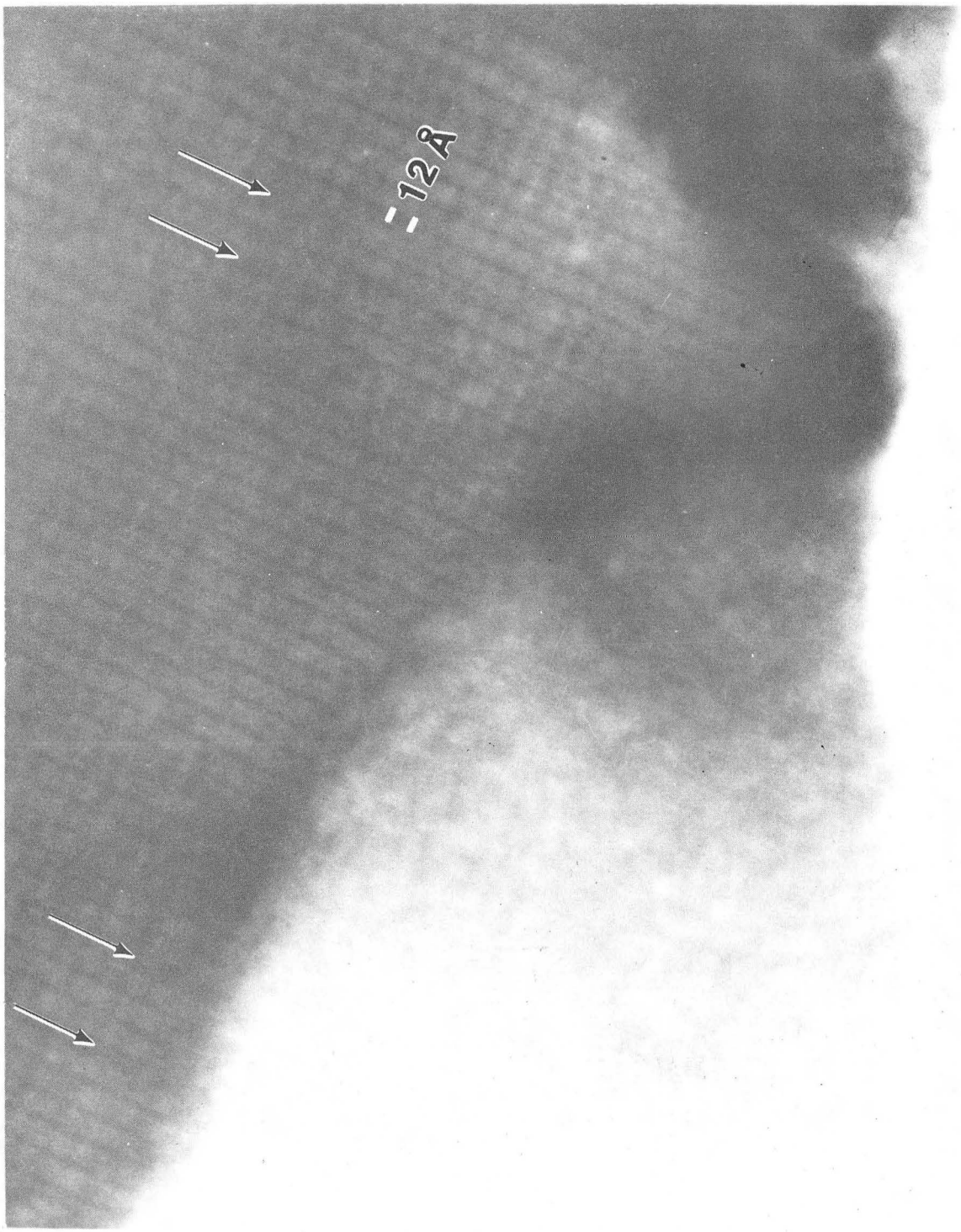

XBB 8110-9274A

Fig. 11

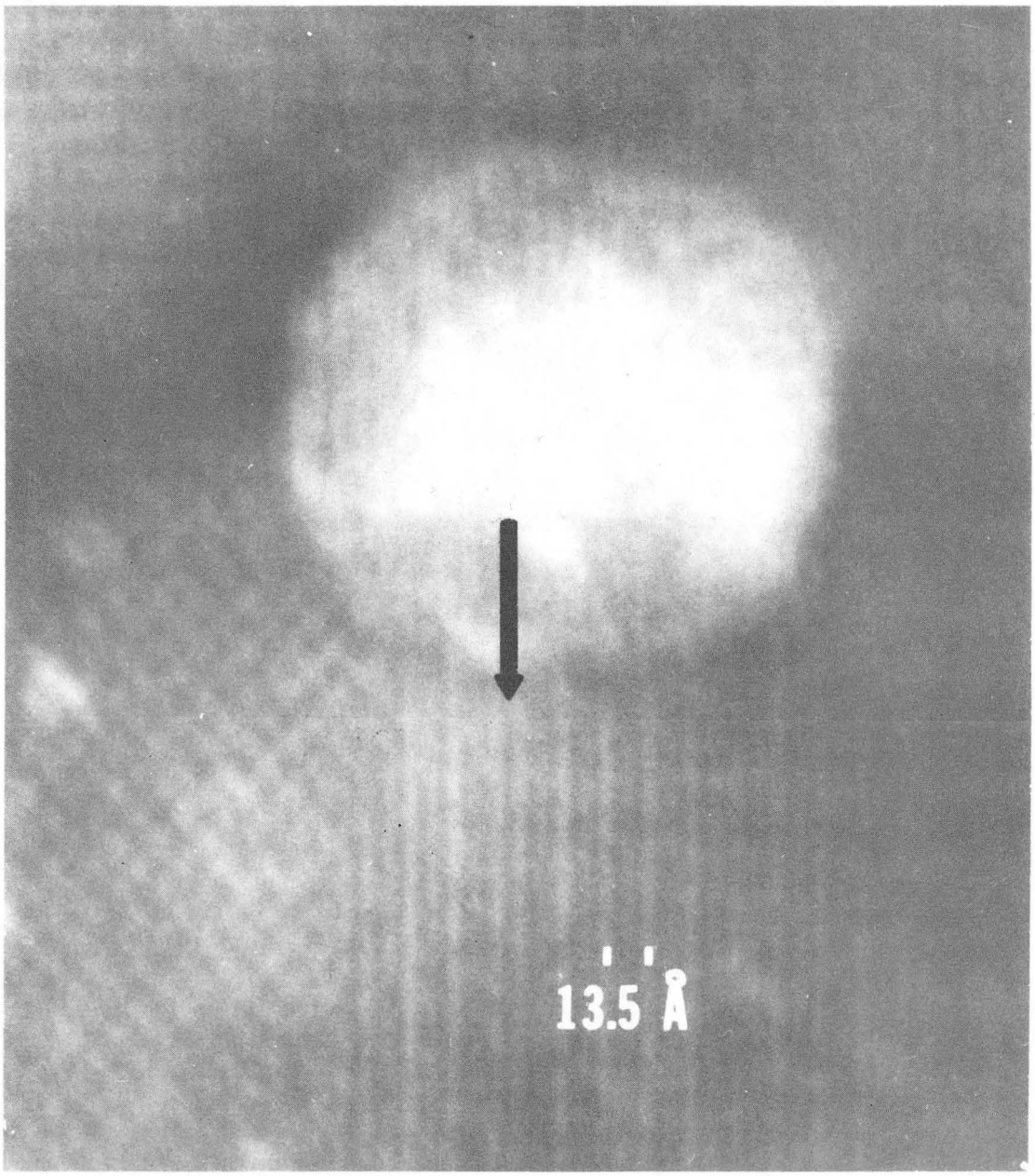

XBB 8110-9594

Fig. 12

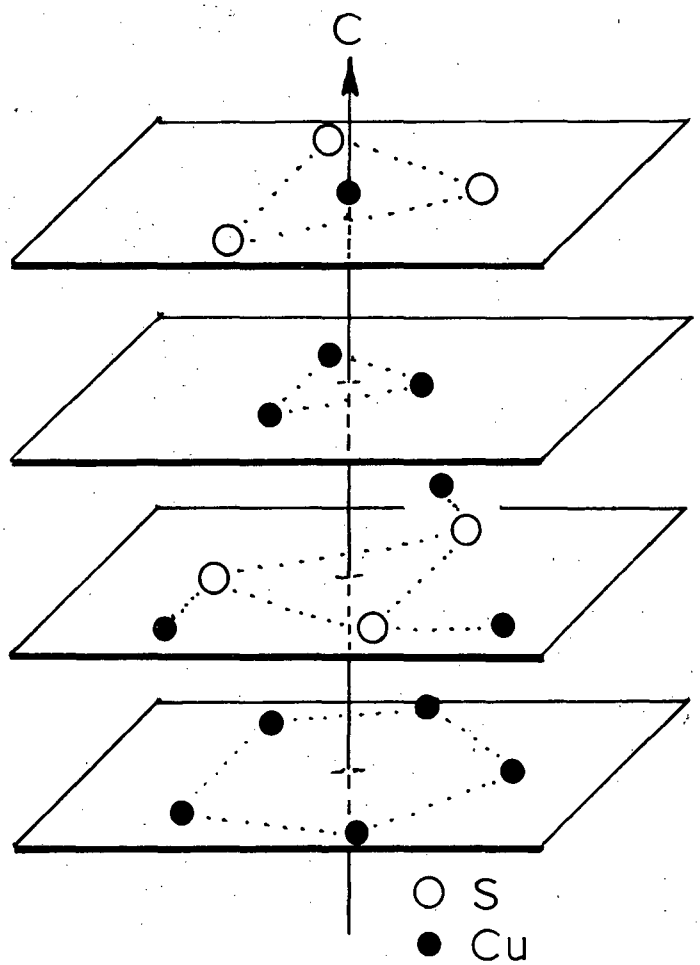

$Cu_{12}S_6$

Chalcocite Building Unit

Fig. 13

XBL 819-7009

THE ARRANGEMENT OF BUILDING UNITS IN CHALCOCITE

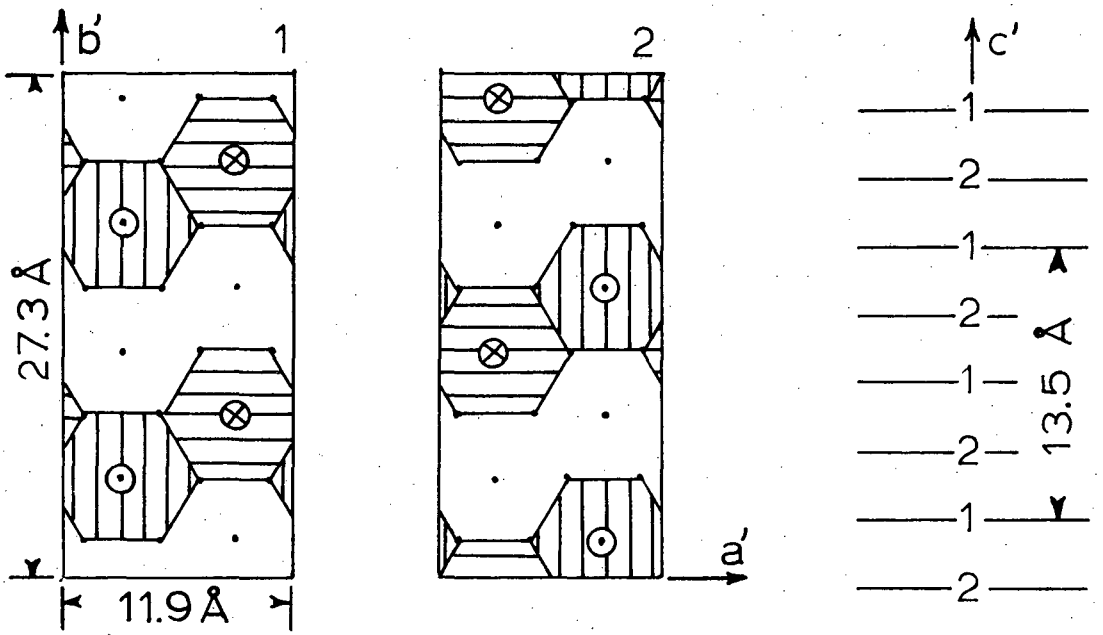

Hexagons represent the 5-Cu layers of the building units. The remainder of the unit is above (⊙) or below (⊗) the indicated plane.

XBL 8110-7087

Fig. 14

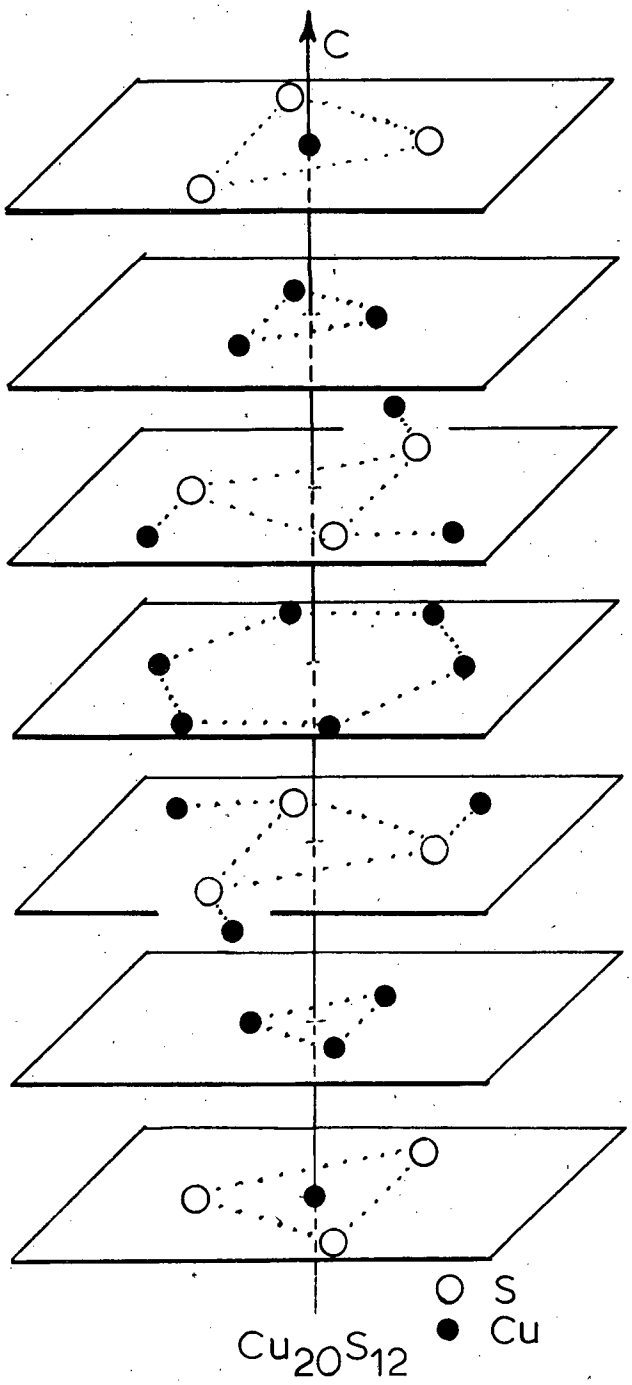

Djurleite: 4 Vacancy Cluster

XBL 819-7008

Fig. 15

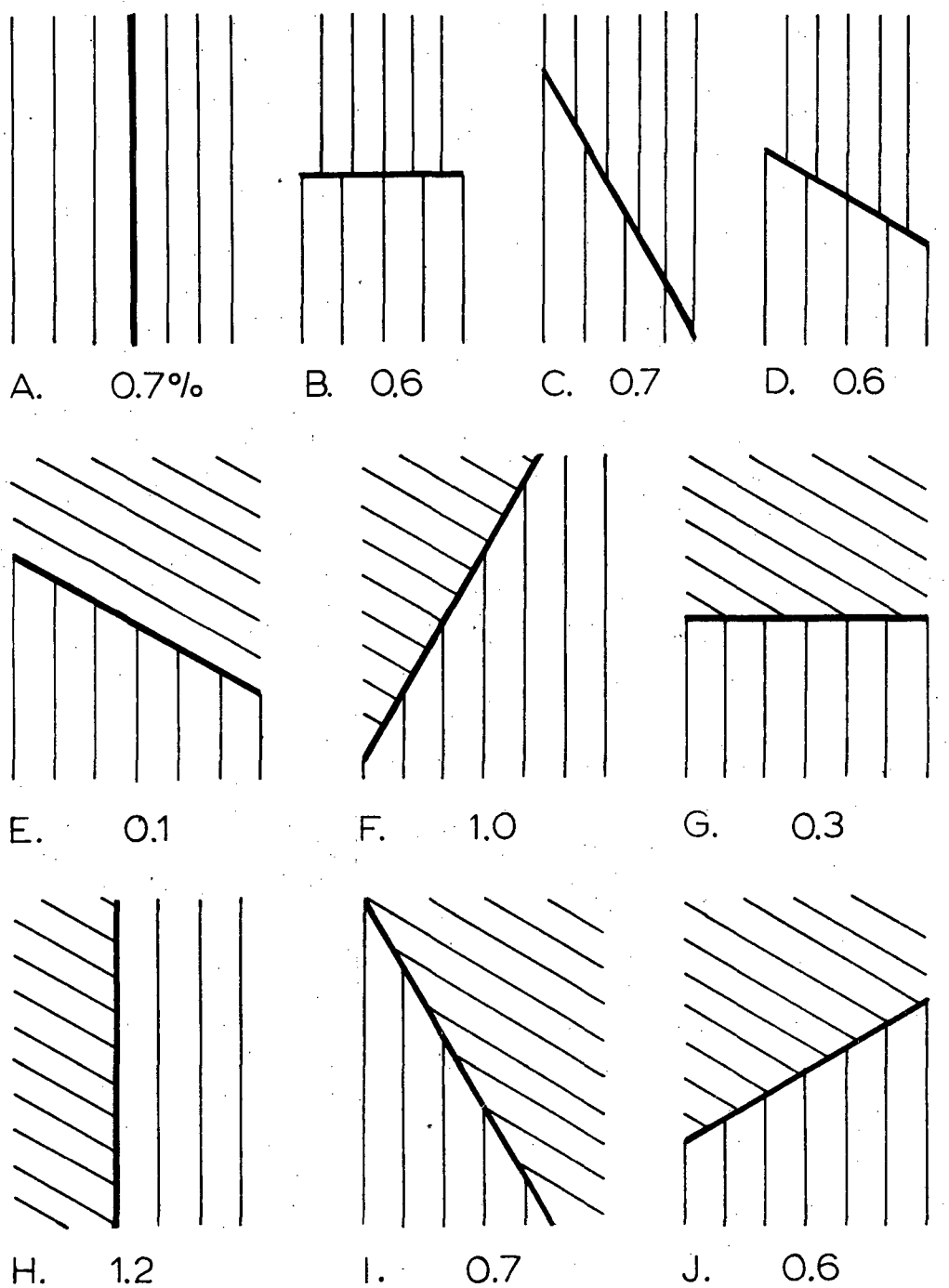

XBL 8110-7086

Fig. 16

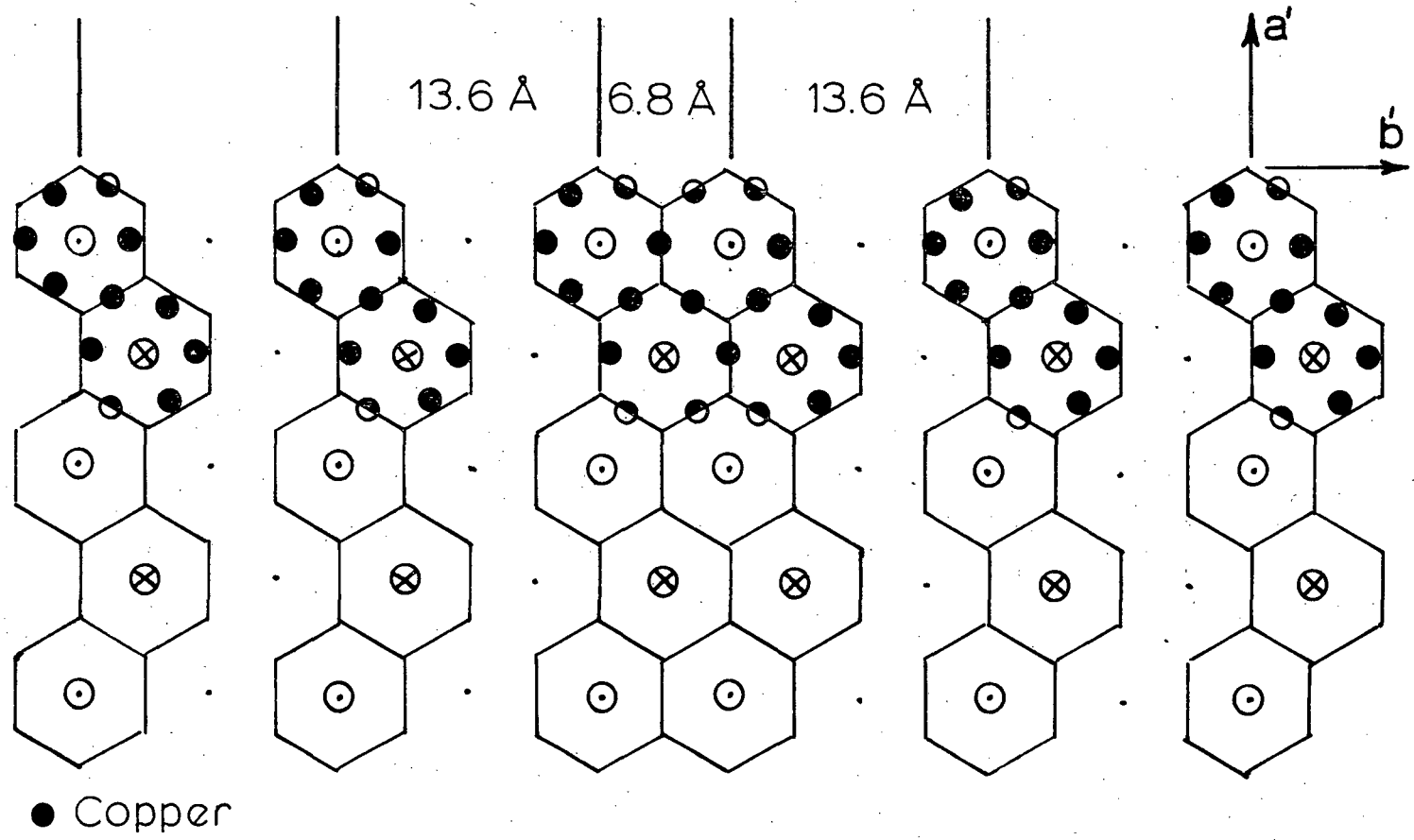

CHALCOCITE 1/4[010] FAULT

XBL 8110-11891

Fig. 17

This report was done with support from the Department of Energy. Any conclusions or opinions expressed in this report represent solely those of the author(s) and not necessarily those of The Regents of the University of California, the Lawrence Berkeley Laboratory or the Department of Energy.

Reference to a company or product name does not imply approval or recommendation of the product by the University of California or the U.S. Department of Energy to the exclusion of others that may be suitable.

TECHNICAL INFORMATION DEPARTMENT
LAWRENCE BERKELEY LABORATORY
UNIVERSITY OF CALIFORNIA
BERKELEY, CALIFORNIA 94720